8-2019

# Fabrication of Resistive Thermo-Optic Heaters on Silicon Photonic Integrated Circuits

Venkatesh Deenadayalan
vd8856@rit.edu

# Fabrication of Resistive Thermo – Optic Heaters on Silicon Photonic Integrated Circuits

Venkatesh Deenadayalan

August 2019

# FABRICATION OF RESISTIVE THERMO – OPTIC HEATERS ON SILICON PHOTONIC INTEGRATED CIRCUITS

VENKATESH DEENADAYALAN

AUGUST 2019

---

A THESIS SUBMITTED IN PARTIAL FULFILLMENT
OF THE REQUIREMENTS FOR THE DEGREE OF

MASTER OF SCIENCE

IN

MICROELECTRONIC ENGINEERING

---


KATE GLEASON COLLEGE OF ENGINEERING
DEPARTMENT OF ELECTRICAL AND MICROELECTRONIC ENGINEERING

# FABRICATION OF RESISTIVE THERMO – OPTIC HEATERS ON SILICON PHOTONIC INTEGRATED CIRCUITS

VENKATESH DEENADAYALAN

---

COMMITTEE APPROVAL

---

Dr. Stefan Preble, Advisor
Professor and Principal Investigator, RIT — Date

---

Dr. Robert Pearson, Committee Member — Date
Microelectronic Engineering Program Director, RIT

---

Dr. Dale Ewbank, Committee Member — Date
Senior Lecturer, RIT

---

Dr. Paul Thomas, Advisor — Date
Senior Process Engineer, Akoustics

---

Dr. Sohail Dianet
Electrical and Microelectronic Engineering Department Head — Date

---

KATE GLEASON COLLEGE OF ENGINEERING
DEPARTMENT OF ELECTRICAL AND MICROELECTRONIC ENGINEERING

## ACKNOWLEDGMENTS

I would like to acknowledge and thank everyone who has stood by my side, playing a crucial role throughout this journey. I would like to start by thanking my advisors and committee members - Dr. Stefan Preble, Dr. Robert Pearson, Dr. Paul Thomas, and Dr. Dale Ewbank for their immense support and guidance throughout my time at RIT. Special thanks to Matthew Van Niekerk, the current (and past) members of the RIT Integrated Photonics Group who have been of great help in teaching new things and being a source of inspiration till now. Secondly, I would like to thank my family who have been giving constant support, allowing me to be independent in all my life endeavors. A very kind and special thanks to Christopher O' Connell (Member of Technical Staff, MIT Lincoln Labs) for all his late-night thoughtful and life discussions in the MicroE graduate students' office and Thomas Wilhelm (PhD., RIT) for all his weekend efforts to stay with me in the clean room, allowing me to complete my fab work. They have been nothing short of good friend-mentors. Without them and my friends in my apartment community, my Master's experience at RIT wouldn't have been so much fun. I would also like to thank the Process Engineers at RIT - Sean O'Brien and Patricia Meller for guiding me through all the processing related queries and the SMFL technicians John Nash, Bruce Tolleson, Rich Battaglia for constantly being available to fix tools and being good company inside the clean room.

# Contents

# List of Figures

# List of Tables

# ABSTRACT

A reliable process for the fabrication of active heater components on passive silicon photonic integrated circuits is presented in this thesis. The heater components enable modulation of the photonic circuits' optical response through the concept of Joule heating. This thesis proposes and successfully establishes an optimized process that can be entirely carried out in an academic clean room facility. The entire cycle of design, simulation and modelling, fabrication and testing is covered. Target lithographic resolution of 300 nm was achieved through process optimization (using a spin on carbon hard mask) by using i-line 365 nm lithography. A very good resolution supported by a near-uniform silicon etch enabled successful fabrication and testing of 30 chips (out of the total 36 chips (~80%)) on a 6" wafer. The second target was the successful demonstration of thermal tuning capabilities using a resistive metal heater made from 50 nm Titanium and150 nm Aluminum (bi-layer). A full FSR (Free Spectral Range) shift of 7 nm was measured on a 400 nm double-bus ring resonator (without modulation) and a complete 7 nm shift was achieved on the same circuit with a power supply of 6V at resistance of ~700Ω. For a 6dBm (3.98 mW) laser supply, a -25 dBm (0.003 mW) output was measured on a basic loop-back circuit with a propagation loss of -28 dBm. The testing results in this thesis are supported by images from optical microscopes, Scanning Electron Microscopy (SEM) and simulations from Lumerical MODE, DEVICE, FDTD and INTERCONNECT solutions.

# I. Introduction and Motivation

The integration of the current generation of microelectronic devices and optics seems inevitable with the ever-increasing industry demands and the soon-to-saturate Moore's law. Alternative technologies which provide high speed connectivity, smaller dimensions and manufacturing reliability seem to be the requirements of this techno-century. Integrated electro-optic technologies have already started to revolutionize telecommunications and high-performance computing sectors with demonstrated terahertz communication capabilities. A very important advantage is that, established chip manufacturing and communication giants like Intel, GLOBALFOUNDRIES and Cisco have dedicated R&D facilities and fab spaces to manufacture photonic devices to cater to next-gen requirements. This avoids the need for setting up dedicated investments and paves the way for manufacturing through re-use of existing equipment and technologies.

Silicon photonics can be best described as the technology that enables propagation and modulation of light through silicon based electro-optic components to realize high speed data transmission. In the current "more than Moore" era, integrated silicon photonics is finding increased applications in the fields of telecommunications, RADAR and LiDAR using LASERs, biomedical engineering, computing and many other demanding sectors.

This thesis is expected to provide the fabrication foundation for the academic photonic course curriculum that is currently being developed at RIT that enables creation of a workforce that is equipped to understand design, modelling, fabrication, testing and packaging of silicon photonic integrated circuits.

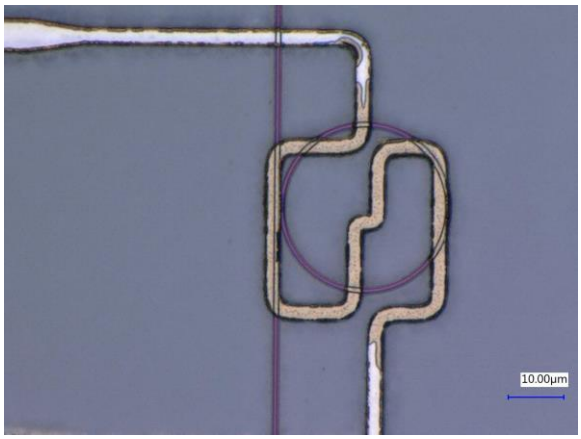


**Figure 1.1**: Integrated resistive ring heater on a single-bus ring resonator circuit

A photonic circuit was originally designed to filter out a specific wavelength/band, might not be able to perform as expected because of fabrication variations. In such a case, redesigning a circuit to accommodate fabrication losses, including manufacturing variations and other requirements seems practically impossible. With modulation capabilities, the circuit can be made to operate as expected by reconfiguring the light modes inside the waveguide by manipulating the effective index of the propagating modes.

Modulation through heat is one of the less desired functionalities of an active photonic circuit. There are many current generation modulation techniques like electro-optic, MEMS actuation etc. available because of thermal tuning requirements and effects like more power consumption, thermal expansion, stress and undesired circuit resistances. Optically, this could trigger unwanted modal responses by causing indeterministic refractive index

changes. In this thesis, we try to understand the effects and get clarity on the optical response of the thermally tuned waveguides and the many other circuits that were fabricated. Also, the experiments would also provide a good estimate on the various processing techniques for example, the cladding, metal layer and isolate the incompatible fabrication combinations for future academic research

## 1.2 Materials in Photonics:

One of the important reasons for using silicon as a photonic material is its ability to propagate light by the property of total internal reflection. It is required that a waveguide material of refractive index higher than that of glass 1.45 ($SiO_2$) is required to allow light to propagate i.e. the difference in refractive indices between the core and the cladding allows total internal reflection. The critical angle can be defined as the angle of incidence at which the angle of refraction is at 90° when the light ray is travelling from an optically denser medium (silicon) into a rarer medium. For silicon, the critical angle is 24.89°. This means that any angle equal or greater than the critical angle (lesser than 90°) allows light to stay and propagate within the silicon.

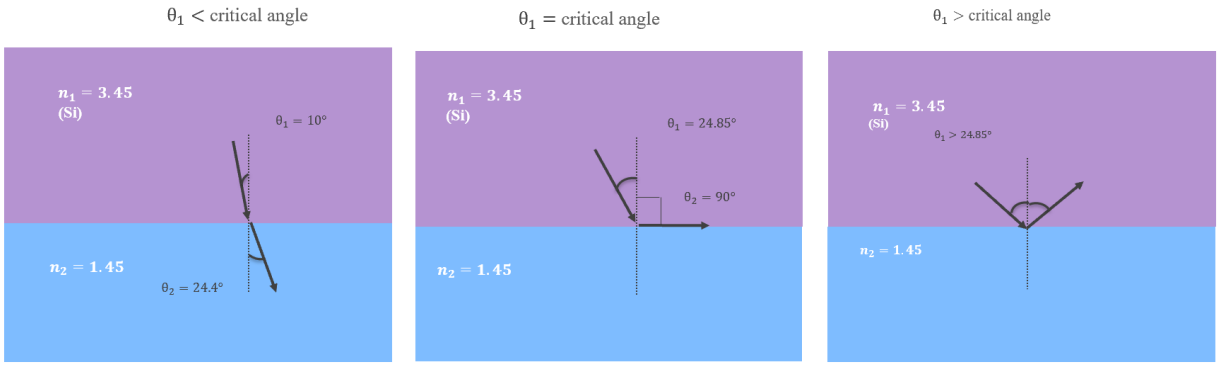


**Figure 1.2:** Total internal reflection and critical angle

The critical angle can be calculated from Snell's law of reflection.

$$\theta_c = sin^{-1}\left(\frac{n_2}{n_1}\right) \quad (1.1)$$

Where, $n_2$ is the refractive index of glass and $n_1$ is the refractive index of silicon. Practically, any material with a refractive index higher than that of 1.45 and is transparent at telecommunication wavelengths can be used as a photonic material.

**Why 1550 nm wavelength?**

The optimal telecommunication wavelengths are between 1260 nm and 1625 nm. This range is further divided into O, E, S, C, L bands and these wavelengths are characterized by lower transmission losses because of lower absorption and scattering effects compared to other wavelengths. In the early 80s, single mode optic fibers with 0.2 dB/Km transmission losses at 1550 nm were developed and has been in use for efficient communication since then. For this thesis work, a 1550 nm laser is being used to couple light into the photonic circuits.

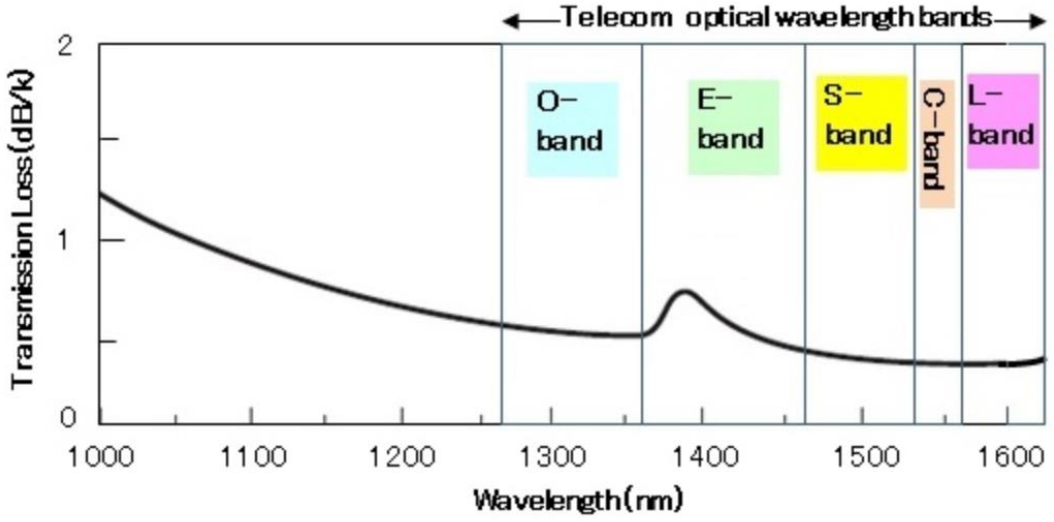


**Figure 1.3:** Bands in fiber optic communication [1]

## 1.3 Modes in Fiber Optics

A typical optic fiber has a core (refractive index $n_1$), surrounded by a cladding ($n_2$) which is covered by a polymer coat. When the difference in the refractive indices between the core and cladding is large, or in situation where the core radius is larger than the wavelength of light that is being propagated, the fiber supports multi-mode propagation. Ideally total internal reflection does not occur for all angles that are in the interval of $\Theta_C^\circ$ and 90° but only at certain specific angles and each of these angles can correspond to a mode. In multi-mode fiber, it can be assumed that light rays propagate at all angles that are within the specified interval and can give rise to too many optical modes.

The problem with using multi-mode fibers is loss through inter-modal dispersion or pulse broadening effect which is described below:

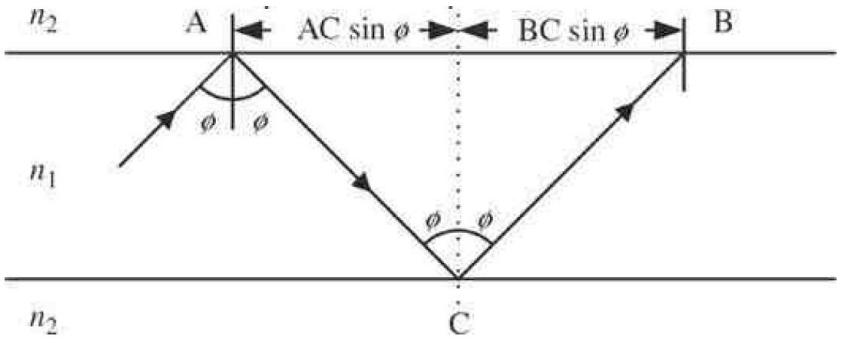


**Figure 1.4:** Ray Diagram inside a multimode optical fiber [2]

Consider a pulse that is being transmitted from one end of the fiber to the other. The light ray is making an angle θ with the core axis of the fiber and is travelling a distance AB in time t (Eqn. 1.2).

$$t_{AB} = \frac{AC+CB}{V_1}; t_{AB} = \frac{AB}{\frac{C}{n_1}sin\theta} \quad \text{(Eq.1.2)}$$

Where, $V_1$ is the velocity of light inside the core and can be denoted by $3x10^{-8}$ $ms^{-1}/n_1$, where $n_1$ is the refractive index of the core. Let us consider ACB triangle in Fig. 1.4 as a single unit. Let x be the total length that the pulse/light ray needs to traverse and us assume that the entire length is made up of T units.

$$t_x = \frac{T \times AB \times n_1}{C\ sin\theta} \quad \text{(Eq. 1.3)}$$

$$t_x = \frac{n_1 \times x}{Csin\theta} \quad \text{(Eq. 1.4)}$$

As mentioned earlier, multimode fibers support propagation of multiple modes within the angle interval of $\theta_c^\circ$ to 90°. At 90°, the light ray grazes along the axis of the core and takes the shortest time to complete the entire length. The time taken by this ray can be given as,

$$t_{min} = \frac{n_1 \times x}{Csin90} = \frac{n_1 \times x}{C} \quad \text{(Eq. 1.5)}$$

When the angle of incidence is equal to the critical angle, the ray takes the longest time to traverse the entire length since the ray will be undergoing maximum number of total internal reflections. In this case, the time taken by the ray is,

$$t_{max} = \frac{n_1 \times x}{Csin\theta_c} = \frac{n_1^2 \times x}{Cn_2} \quad \text{(Eq. 1.6)}$$

When the ray makes an angle $\theta$ in between the interval of $\theta_c^\circ$ and 90°, the time taken should lie in-between $t_{min}$ and $t_{max}$.

The pulse that is sent at the input end, excites all the modal rays that are in-between $\theta_c^\circ$ and 90° and the rays arrive at the destination end at a time interval denoted by ΔT.

$$\Delta T = t_{max} - t_{min} = \frac{n_1^2 \times x}{c n_2} - \frac{n_1 \times x}{c} \qquad \text{(Eq. 1.7)}$$

$$\Delta T = \frac{n_1 x}{c}\left(\frac{n_1}{n_2} - 1\right) = \frac{n_1^2 x \Delta}{c n_2} \qquad \text{(Eq. 1.8)}$$

Where $\Delta$ is the relative index difference ($(n_1-n_2)/n_1$) and $\Delta T$ is the pulse width at the output end of the fiber. In Fig. 1.5, $T_B$ is the interval between the original pulses and the bottom shows the pulse broadening effect due to $\Delta T$ in a multi-mode fiber.

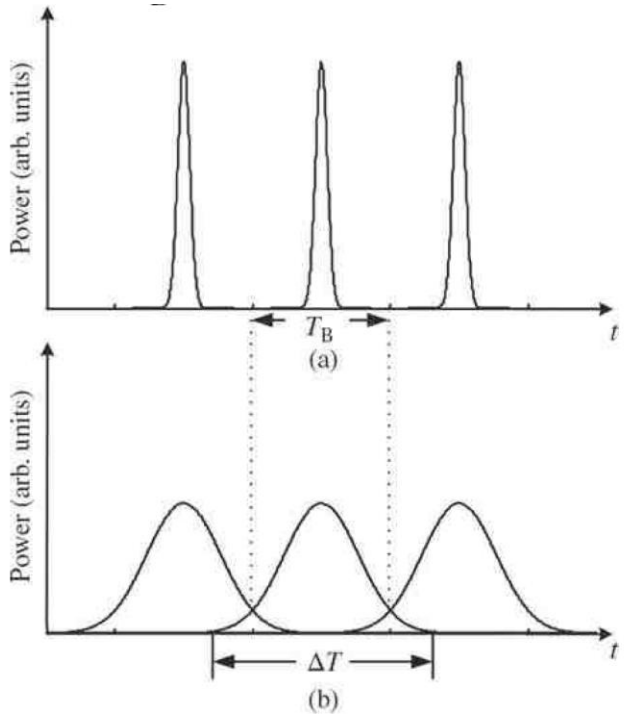


**Figure 1.5:** Individual pulse tracking in the absence of other pulses at the input (a) and at the output (b) [2]

Hence, to achieve maximum transmission over longer distances and reducing modal dispersion (no overlapping pulses) with minimal loss with the smaller core diameter, single mode fibers are used. They are the requirement for high speed transmission and better

bandwidth accommodation. This can be realized by using fibers with reduced ($n_1 - n_2$) and by having the core diameter comparable to the wavelength of the light that is used.

# II. Optics for Photonics

## 2.1 Fermat's principle of least time: Analysis on reflection and refraction

Reflection and refraction are two events which occur when light travels from one medium to another with a different refractive index.

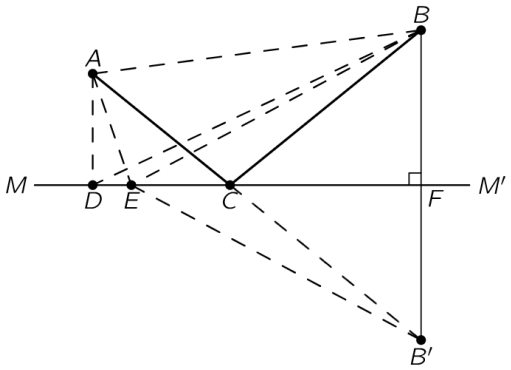


**Figure 2.1:** Illustration of reflection and refraction according to Fermat's principle of least time [2]

In Fig. 2.1, MM' is the mirror. In order to find out the shortest path that allows the light to move from point A to B, an imaginary point B' is constructed which is at the same distance below the mirror as the point B above. Lines EB and CB' are constructed. Since, ∠BFM and BF = FB', we get AE+EB = AE+EB' and EB=EB'; The shortest time the light ray could travel is through the straight-line path ACB'. If ACB' is a considered a straight line, then ∠BCF=∠B'CF=∠ACM, proving that the angle of incidence is equal to the angle of reflection.

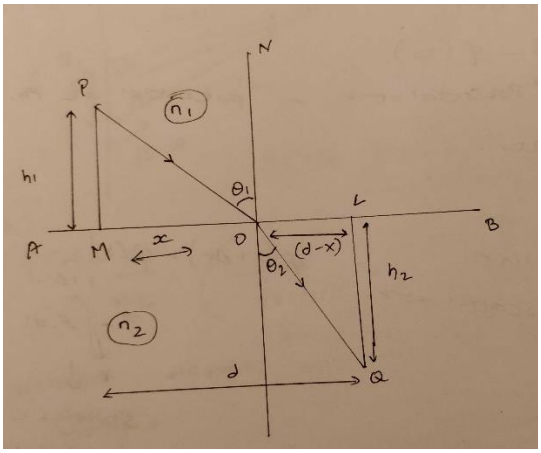


**Figure 2.2:** Ray diagram - Refraction

Refraction is a phenomenon which causes the light ray to bend towards the normal to the interface, when it travels from a denser medium into a rarer medium. In Fig. 2.2, there are two media – air and water. Let us assume that light travels slower in water than in air by a factor of n.

Total time taken by the ray to move from P to Q is given by

$$t = \frac{PO}{V_1} + \frac{OQ}{V_2} = \frac{\sqrt{h_1^2+x^2}}{V_1} + \frac{\sqrt{h_2^2+(d-x)^2}}{V_2} \qquad \text{(Eq. 2.1)}$$

According to Fermat's principle, since the light takes the shortest route, we set the derivate of time with respect to x to be 0 i.e. dt/dx=0, or the change associated with a very small change in time over a very small change in position is 0.

$$\frac{dt}{dx} = \frac{1}{v_1}\frac{2x}{2\sqrt{h_1^2+x^2}} + \frac{1}{v_1}\frac{2(d-x)(-1)}{2\sqrt{h_2^2+(d-x)^2}} = 0 \qquad \text{(Eq. 2.2)}$$

$$0 = \frac{1}{v_1}\frac{OM}{OP} + \frac{1}{v_1}\frac{OL}{OQ} \qquad \text{(Eq. 2.3)}$$

$$0 = \frac{1}{v_1}Sin\theta_1 + \frac{1}{v_1}Sin\theta_2 \left[and\ v_1 = \frac{C}{n_1}, v_2 = \frac{C}{n_2}\right] \qquad \text{(Eq. 2.4)}$$

$$n_1 Sin\theta_1 = n_2 Sin\theta_2 \qquad \text{(Eq. 2.5)}$$

Eqn. 2.5 is Snell's law which forms the basic principle of total internal reflection.

## 2.2 Bragg's diffraction condition

Bragg's grating filters are used in various optical devices to perform wavelength selective operations. The grating couplers which are used for the purpose of transmitting light in and out of the circuits, operate on this principle of diffraction. Diffraction is an optical phenomenon that occurs when light tries to propagate through a very confined slit/ even an obstacle. The diffraction point eventually becomes the secondary source for the propagating/diffracting light. The diffraction gratings in the coupler should be having a period (pitch) comparable to the wavelength of the light that is being used. There are certain criteria defined by the Bragg's condition, that need to be followed while designing the grating couplers for efficient light coupling and to avoid any back-reflections caused from second order diffraction of the scattering light. These back reflections, in addition to contributing to loss, cause undesirable interferences to the incoming light that goes into the circuit. A Bragg grating is designed by periodically changing the core of waveguide. In the case of grating coupler designs in this thesis, this variation in refractive index (graded index) is achieved by having oxide in-between the silicon. When the grating period is exactly half of the input light's wavelength, the light will be reflected coherently (more directional) and will eventually make a large reflection. This condition is called Bragg's grating condition (in Eq. 2)

$$\lambda_B = 2\mathrm{A}n_{eff} \qquad \text{(Eq. 2.6)}$$

Where $\lambda_B$ is the wavelength of light that is reflected by Bragg's condition and it is clearly the function of the grating period A and effective index $n_{eff}$. The Bragg's wavelength is typically 2x or 3x times the periodicity of the gratings.

In a periodic grating coupler, each grating which has a pitch equal to the wavelenght of light, each individual grating acts as a source of scattering and causes a spherical wave front of interfering waves which is reflecting upwards from the gratings as seen in Fig. 2.2 d. This first order diffraction of the grating given by Bragg's condition is given by:

$$\beta - k = k_z \qquad \text{(Eq. 2.7)}$$

Where β is the propagation constant ($\beta = \frac{2\pi n_{eff}}{\lambda}$) and $k = \frac{2\pi}{A}$ and $k_z$ is the projected wave vector of the incident light mode ($k_z = \frac{2\pi}{\lambda} sin\theta$), where θ is the angle of the fiber with respect to the surface normal of the grating as shown Fig. 2.2. Coupling light at a higher positive angle (shown in Fig. 2.2 a) would conveniently avoid any second order back-reflections.

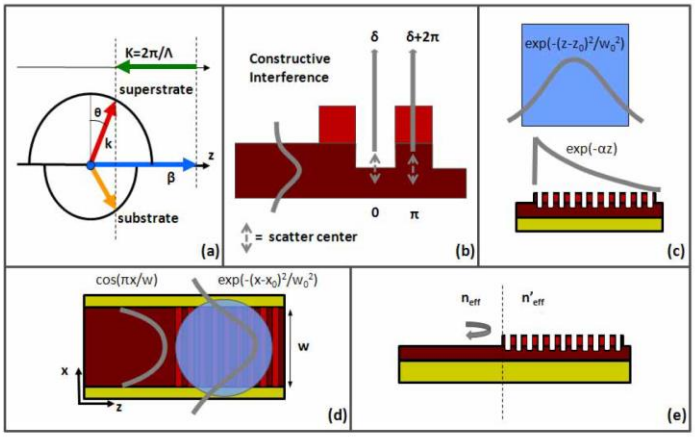


**Figure 2.1**: Illustrations of grating coupler design and operation (satisfying Bragg's condition) [3]

## 2.3 Effective Index and Group Index:

Effective index is an inherent parameter that can be used to characterize the waveguide performance. It can be best explained as the average value of refractive indices calculated at various higher order modes.

$$n_{eff} = n_1 + n_2(\lambda - \lambda_0) + n_3(\lambda - \lambda_0)^2 \qquad \text{(Eq. 2.8)}$$

As the wavelength of light decreases, the effective index of the waveguide increases for increasing width. This is because the light travels at varying speeds at different wavelengths and the increased light interaction with more silicon surface area. The effective index swept across different waveguide widths with the fundamental and first order modes with single mode cut off can be seen in Fig. 2.4. Extrapolating the plot to widths less than 200 nm, the effective index will eventually hit the refractive index of the cladding silicon oxide. This means that the light mode will be concentrated more in the cladding leaving behind a small fraction inside the silicon depending on the thickness. This is because the waveguide width has direct impact on the conditions that satisfy total internal reflection. Widths greater than the 450 nm will give rise to higher order modes/multi modes which are not ideal for the process.

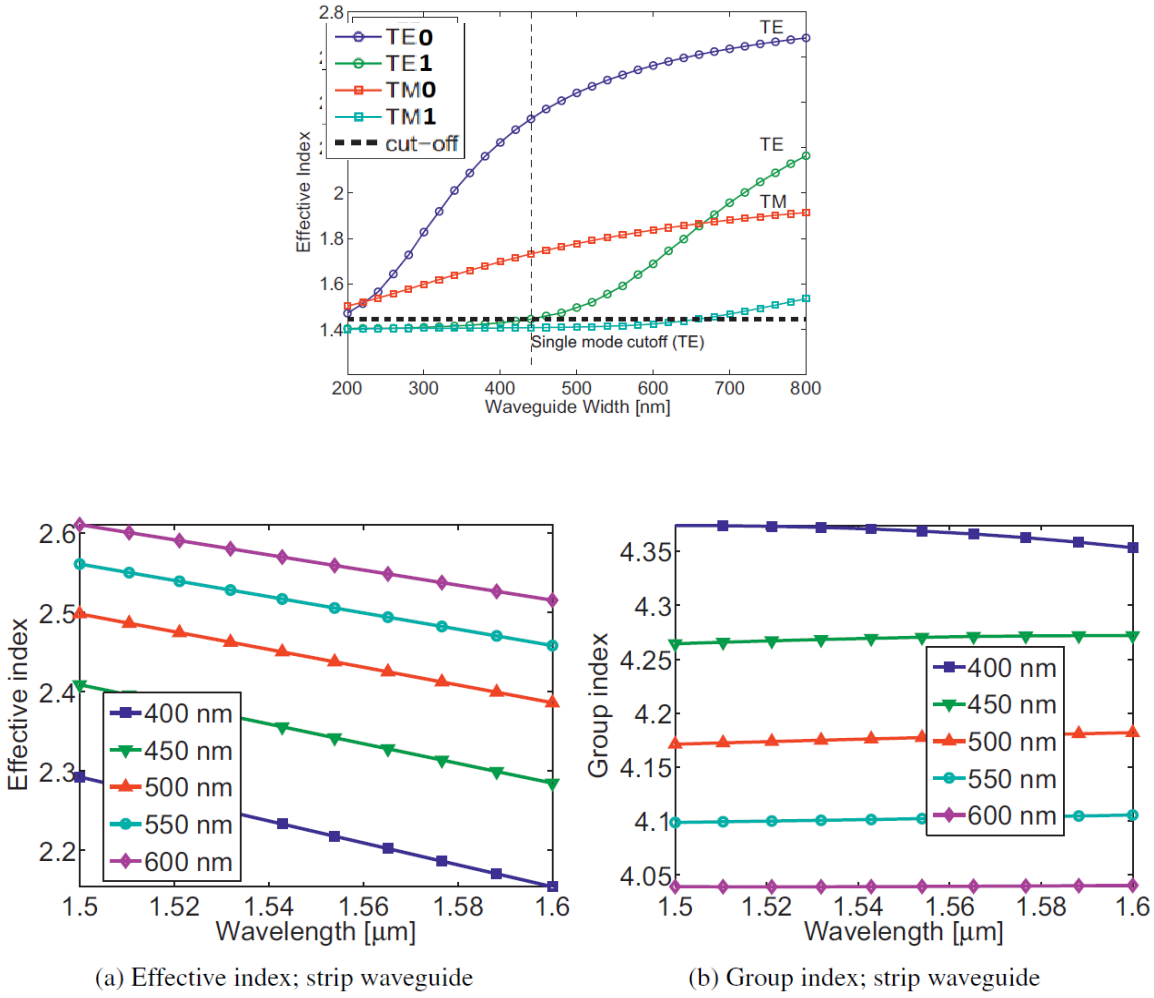


**Figure 2.4:** Single mode cutoff at 450 nm for TE and TM (fundamental and 1st order mode) (top), Effective and Group index plots for TE polarized light (bottom) [4]

Group index is another parameter of the photonic component/circuit. The effective index $N_{eff}$ of the waveguide at the desired band of wavelength is used in the calculation of group index. The resulting group index value is used in determining how fast a dataset is being transmitted via the waveguide which is the group velocity.

$$n_g = n_{eff} - \frac{dn_{eff}}{d\lambda}\lambda_0 \qquad \text{(Eq. 2.9)}$$

Group velocity can be calculated from the effective index as seen in Eqn. 2.9. A typical silicon waveguide 500x220 nm would be having an effective index of 2.44 and a group index if 4.2 at a wavelength of 1550 nm for TE polarized light.

## 2.4 Thermo-optic effects in silicon:

Thermo-optic tuning of silicon photonic structures was one of the very early techniques discovered to induce modulation by changing the refractive index (or effective index) of the silicon waveguide core without a large amount of optical loss. This is made possible by the large thermo-optic coefficient of $1.87 \times 10^{-4}$ of silicon.

Tuning the FSR (Free Spectral Range) to the maximum possible value with minimal power is the requirement of a good thermo-optic heater. This large tuning range allows the photonic circuits to operate over an extended bandwidth.

For example, a ring resonator circuit which was originally designed to filter out 1565 nm wavelength, might not be able to perform as expected because of fabrication variations. In such a case, redesigning a circuit to accommodate fabrication losses, including manufacturing variations and other requirements seems practically impossible. With modulation capabilities, the circuit can be made to operate as expected by reconfiguring the light modes inside the waveguide by changing the effective index of the propagating modes.

When a waveguide is heated up, there is no physical change (expanding/length change) to the it, instead by the principle if Joule heating, the light mode is manipulated. This is done by variation in the effective index (Δn) of silicon.

$$Electric\ field = \frac{E_{input}}{2} e^{(i\beta L + i\pi)} \qquad \text{(Eq. 2.10)}$$

$$\beta L = \pi$$

$$\beta = \frac{2\pi n}{\lambda} => \Delta\beta = \frac{2\pi \Delta n}{\lambda} \quad \text{(Eq. 2.11)}$$

$$\Delta n_{thermo-optic} = 1.87 \times 10^{-4} K \quad \text{(Eq.2.12)}$$

$$Power\ \alpha\ I^2 R \quad \text{(Eq. 2.13)}$$

Joule's law of ohmic heating states that, the Heating power (P) generated by an electrical conductor is directly proportional to the resistance (R ) and square of current ($I^2$). According to this principle, to maximize the heat, a highly resistive metal is used to obstruct the flow of current.

In Eqn. 2.10, $\frac{E_{input}}{2}$ is the amplitude of the electric field and $e^{(i\beta L + i\pi)}$ is the phase component (the π is the additionally produced phase shift). The thermo-optic coefficient of a material determines how well it responds to applied temperature. For silicon the refractive index changes by a factor of per kelvin change in temperature. This thermo-optic coefficient (Eqn. 2.12) is measured at a temperature of 300 K (standard working conditions). Any temperature changes to the silicon waveguide core, by the principle of heat transfer through Joule's resistive heating (Eq. 2.13), would affect the silicon's refractive/effective index, thereby changing its optical properties. $SiO_2$ has a very negligible thermo-optic coefficient so, the transmission through the cladding can be assumed to be the same before and after heat stimulus. While designing a resistive heater, factors like temperature coefficient of the heater metal, silicon thermal expansion, distance of separation between the heater and the waveguide, thermo-optic coefficient of the cladding oxide etc. come into picture. Each of them could be analyzed individually and optimizations can be done to get better results.

# III. Photonic Components and Circuits: Theory and Design

The photonic component variations and the circuit designs for this thesis were carried out using K-layout chip design software. The photonic Process Development Kit (PDK) developed by the members of RIT's integrated photonics group has a broad array of components, layer specifications and very useful backend python (computer program) macros for scripting which were used to build customized circuits. The designs were implemented keeping in mind two major objectives (i) To test the photonic circuits before modulation i.e. without heaters (ii) test with thermal modulation to understand the circuit response. In addition to the designs, the thermal tuning was also simulated virtually to get a mathematical model of the thermal tuning and visualize an accurate optical response of the designed circuits using Lumerical MODE, INTERCONNECT and DEVICE software. The Finite Differential Eigen (FDE) engine runs in a loop and looks for solutions that satisfy the Maxwell's wave equations and outputs the results in the form of modal parameters like effective index, polarization modes etc.

## 3.1 Photonic Components: Grating Couplers and Waveguides

The two major components for building a photonic circuit are (a) Grating coupler (b) Waveguide

### (i) Grating couplers

Vertical and edge coupling are the two main ways to get the light from fiber array couple into and out of the photonic circuits (via the diffraction gratings in the coupler) as shown in Fig.

3.1. Vertical coupling is more lossy and less efficient compared to edge coupling as the former technique will always involve light coupling from a height 'h' from the couplers. Whereas, in case of edge coupling, the light can be transmitted/coupled from very close proximity onto the edge couplers which will reduce the coupling loss to a great extent. Another major disadvantage of using a grating coupler is that the bandwidth of operation is very less (~50 nm) and should have the light incident at a specific angle (30° in this thesis). Light when it is incident on these gratings, they undergo diffraction, scattering and continue to propagate through successive gratings. This is based on Bragg's grating condition and the principle of operation is explained in chapter 2

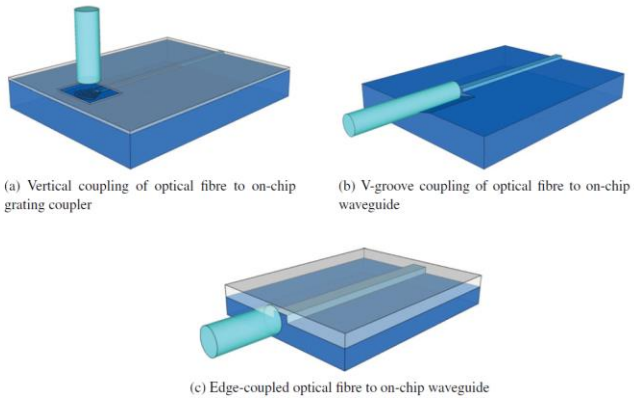


**Figure 3.1:** Light coupling methods [4]

In this thesis, grating couplers which have a duty cycle of 50% i.e. there is 50% silicon and 50% oxide in the grating region are being used. This would provide a combined $n_{eff}$ of (2.44+1.44)/2 = 1.94. The gratings are curved to focus the incoming light beam into the waveguide.

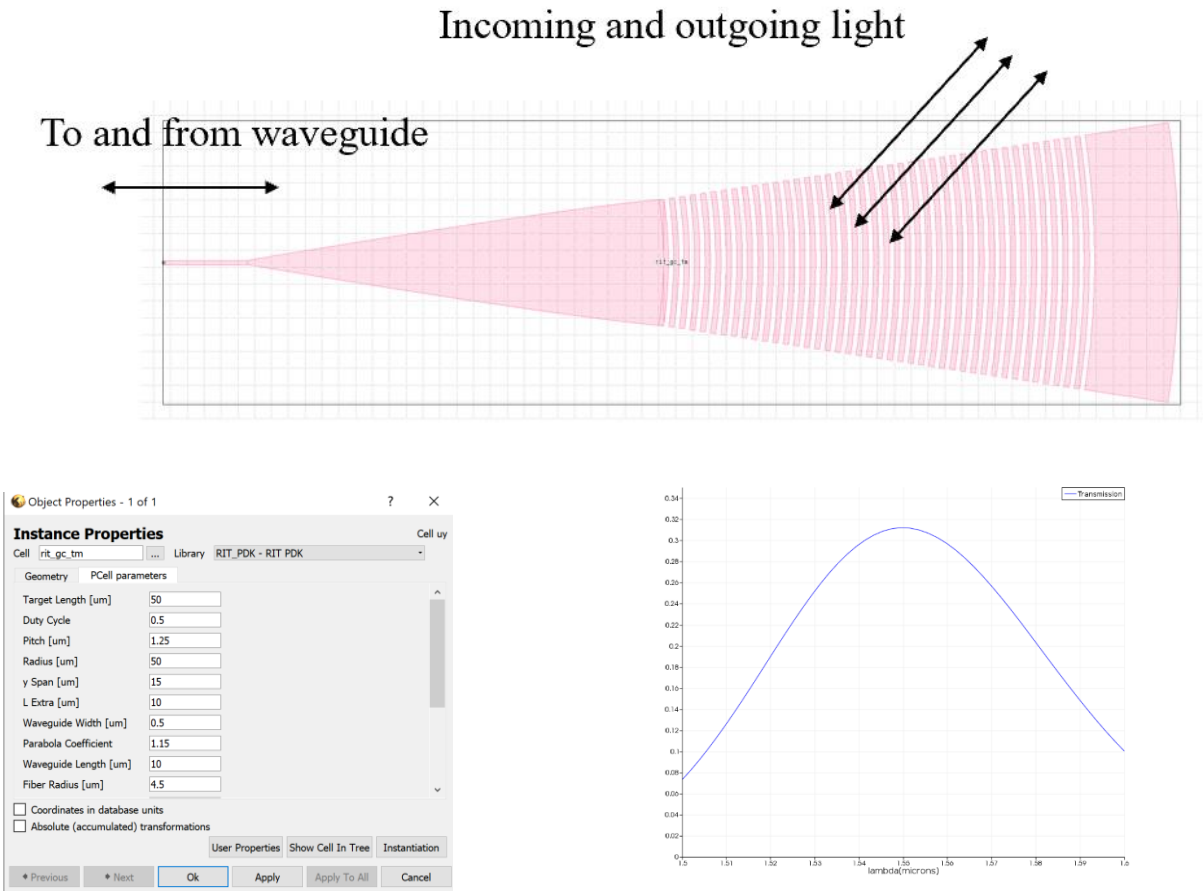


**Figure 3.2:** Design and specifications of a grating coupler used in this thesis (for all designs) (top and bottom left), grating coupler response showing maximum transmission around 1550 nm (bottom right) [4].

## (ii) Waveguides and Bends:

Waveguides work like an optic-fiber cable. They guide light by the principle of total internal reflection. As much as waveguide dimensions are critical in the design and fabrication of straight-waveguide photonic circuits, their bends also play a vital role in allowing lossless light propagation. One of the major advantages of designing and fabricating strip waveguides (the most common type) is that they allow tighter bends with minimal loss because of their

increased effective index. When the bend radius is too tight, say ~2.5 μm or less, the mode will be forced towards the edges causing some of the light to radiate out into the evanescent field (the field surrounding the waveguide). The bends can be engineered to filter out modes (if only TE modes are needed, the bend radius for the waveguides can be kept very tight, say 5 μm. TM requires a much larger bend radius). The two major losses that need to be considered while designing a bend are the radiation and the mode conversion losses cause by misalignment of the modes as the light in the waveguide turns from one direction to another through the bend. The third loss is the -3 dB waveguide propagation loss or the scattering loss due to roughness variation, which is assumed to be a standard loss for all waveguides. Among these three losses, the transmission loss/ the mode conversion loss is the most critical one because the light takes two turns inside a bend (i.e. undergoes two orientation changes) this can be seen in Fig. 3.3

$$Total\ Bend\ loss = \frac{2\pi R}{4}\ (Radiation\ loss + Transmission\ loss + Propagagation\ loss)\ dB$$

These bend losses can be reduced by designing larger bends and changing the orientation of the bend. While designing and simulating the waveguide bends, they are implemented as multiple closely packed straight-line structures that are expected to be curved. Hence, during the lithography process, it attempts to create the curvature but, they are just dense boxed structures that appear to be curved.

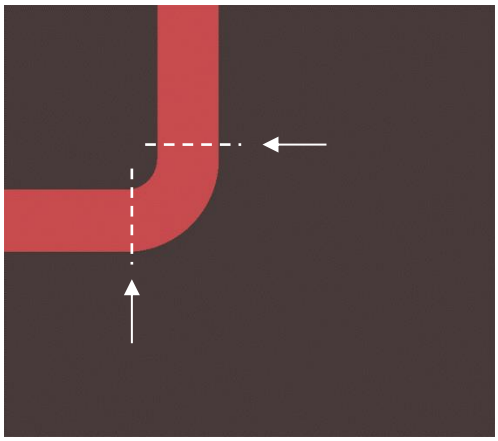

**Figure 3.3:** Waveguide bend showing two directional turns [4]

dB to ratio conversion table

| dB | Amplitude ratio | Power ratio |
|---|---|---|
| -100 dB | $10^{-5}$ | $10^{-10}$ |
| -50 dB | 0.00316 | 0.00001 |
| -40 dB | 0.010 | 0.0001 |
| -30 dB | 0.032 | 0.001 |
| -20 dB | 0.1 | 0.01 |
| -10 dB | 0.316 | 0.1 |
| -6 dB | 0.501 | 0.251 |
| -3 dB | 0.708 | 0.501 |
| -2 dB | 0.794 | 0.631 |
| -1 dB | 0.891 | 0.794 |
| 0 dB | 1 | 1 |
| 1 dB | 1.122 | 1.259 |
| 2 dB | 1.259 | 1.585 |
| 3 dB | 1.413 | 2 ≈ 1.995 |
| 6 dB | 2 ≈ 1.995 | 3.981 |
| 10 dB | 3.162 | 10 |
| 20 dB | 10 | 100 |
| 30 dB | 31.623 | 1000 |
| 40 dB | 100 | 10000 |
| 50 dB | 316.228 | 100000 |
| 100 dB | $10^{5}$ | $10^{10}$ |

$$\text{Ratio in dB} = 10 \log_{10}(P_1/P_2)$$

Where, $P_1/P_2$ is the power ratio. For example, for 50 % power ratio equals – 3dB

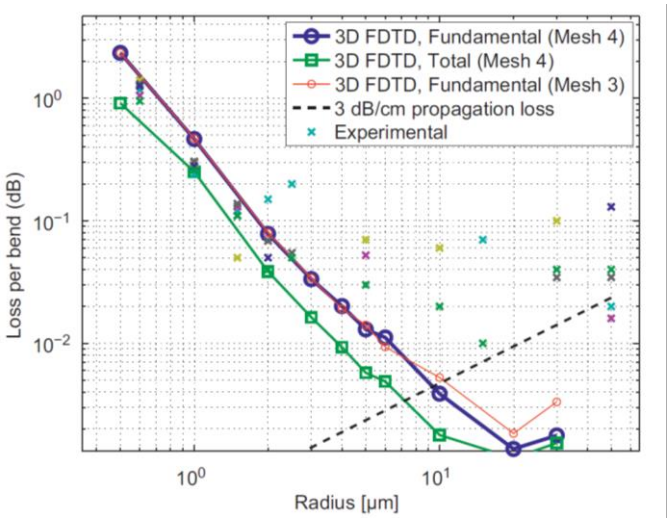


**Figure 3.4**: Decibel - Power ratio conversion chart (left), Different bend losses (right) [4]

The plot in Fig. 3.4 shows a comparison of experimental vs Lumerical MODE simulations for a 220 x 500 nm strip waveguide with varying bend radii. The optical power transmission which is calculated as the ratio of the output to that of the input and is plotted against the bend radius. The plot shows two kinds of transmission data, Fundamental (power in the

fundamental mode excluding the higher order modes) and the total (total power measured in the output waveguide). From the plot, it is evident that, as the bend radius increases, the radiation and the mode transmission losses are almost non-existent because the light does not see much bending and only the -3 dB propagation loss exists (which is equivalent to a 50% power loss according to equation shown in Fig. 3.4).

Normally, decibel (dB) scale is used for measuring electronic/acoustic signals. It is on a logarithmic scale and helps in measuring very large/ very small values in a math friendly manner. Decibel scale is used in loss/gain plots. While dBm, which is decibel-milliwatts is the power ratio expressed in decibels with reference to 1 mW (milliwatt), is most commonly used in power response (transmission) plots

$$P\ in\ mW = 1\ mW\ x\ 10^{\frac{P\ in\ dBm}{10}} \qquad \text{(Eq. 3.1)}$$

For example, 30 dBm equates to 1000 mW

## 3.2 TE and TM Polarization:

Ideally, in a two-dimensional TE polarized waveguide, the electric field is oriented parallel to the surface if the silicon waveguide. The polarization depends on the thickness of the silicon in combination with the electric field intensity. In a TE wave, the electric field is perpendicular to the direction of light propagation while in a TM wave, the magnetic field is perpendicular. In all the plots/simulations of the waveguide cross sections in the YZ plane, the x component is the direction of propagation of the electromagnetic light wave.

We use TM polarized light for this thesis because the coupling is faster and requires a smaller crossover length compared to TE (refer section 3.3). The gaps need not be too small, and the

coupling can happen even with larger gaps. Through Lumerical MODE simulations it was found that TM modes have greater difference in the effective indices between the odd and the even mode. This essentially means that the coupling coefficient C is greater for TM according to equation.

$$C = \frac{\pi \Delta n}{\lambda} \qquad \text{(Eq. 3.2)}$$

For a TM polarized light, the effective index and the group index for a standard silicon waveguide of 220x500 nm were 1.77 and 3.74 respectively at 1550 nm. The simulations which were done for TM polarized light can be seen in Fig. 3.5.

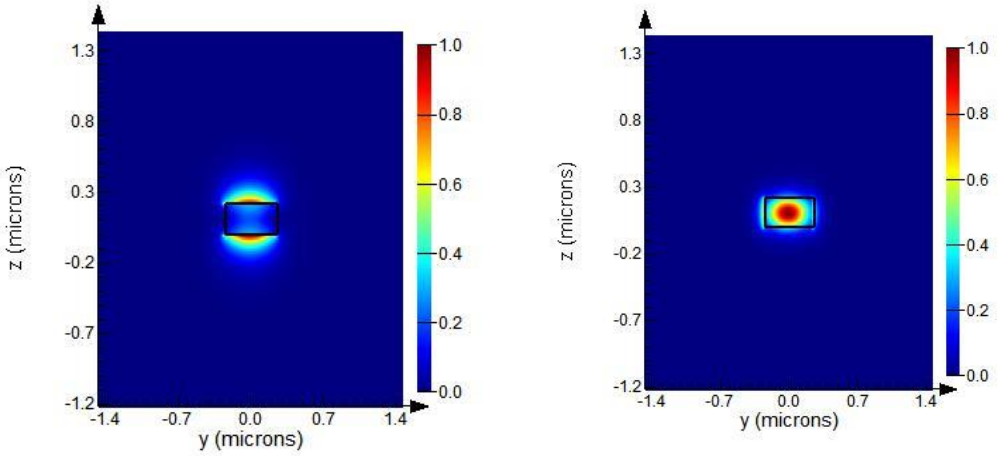


**Figure 3.5:** TM mode showing electric field in z direction (left), TE mode showing electric field in y direction (right)

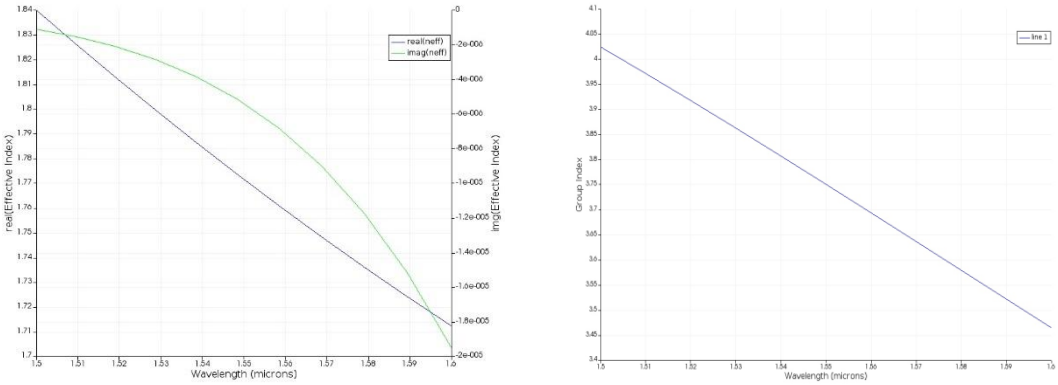


**Figure 3.6:** Effective index and group index plots for a TM polarized wave (Magnetic field (along y direction) is perpendicular to the direction of light propagation)

## 3.3 Directional couplers and Mach-Zender Interferometer Circuits

### (i) Directional Coupler

Any basic photonic integrated circuit would involve the concept of light coupling from one waveguide to another. Light coupling/crossover involves modal superposition (supermodes). A Directional coupler is one of the basic building blocks best used to describe the concept of light coupling. The primary function of a directional coupler is to split and combine light. This is achieved by having two waveguides in parallel to each other and the light couples from one waveguide to another 'cross-over' waveguide according to coupled mode theory (CMT) [43]. This is controlled by the coupling coefficient of the waveguides which in turn is dependent on the length and the separation distance between them. CMT is characterized by the assumption that there are forward and backward travelling modes in a straight waveguide because of modal disturbances. In the case of a directional coupler, the modes that are calculated for individual waveguides in isolation are assumed to couple when they are brought together. This phenomenon is also called as the supermodal interaction where symmetric(even) and asymmetric(odd) modes exist and interact with each other

(tunnel from one waveguide to another) depending on how close the waveguides are positioned.

Fig 3.7 shows the implication of symmetric and asymmetric TM super modal interaction in a directional coupler (green box represents asymmetric/odd (red has an amplitude of 0.8 and blue has an amplitude of -0.8 and blue box represents symmetric/even (both positive)). The ports for this device are labelled $P_1$, $P_2$, $P_3$ and $P_4$. Both the odd and even modes will have different effective indices. This difference in effective indices cause the modes to propagate at varying speeds inside the waveguides and cause back and forth oscillations inside them.

For example, if we send TM polarized source light via port 1 and detect light in port 3 and port 4, there should be 50% split in both the output waveguides. Sending a TE source light via port 1 will cause the TM component to couple quicker into port 3.

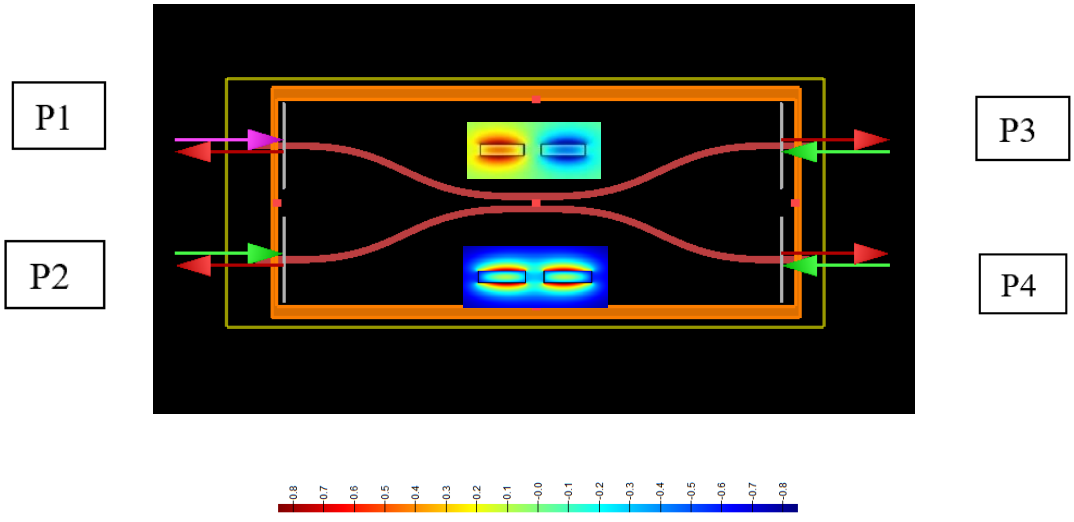


**Figure 3.7:** A 4-port directional coupler

The percentage of power that is coupled from one waveguide to another is given by

$$k^2 = \frac{P_{coupled}}{P_0} sin^2(c.l) \qquad \text{(Eq. 3.3)}$$

Where $P_0$ is the input power through the waveguide, $P_{coupled}$ is the power that is coupled across the directional coupler, c is the coupling coefficient and l is the length of the coupling waveguide. The power coupled from the initial to the coupled waveguide can be given as: where L is the crossover length. So, the response of a directional coupler will vary sinusoidally over a wide range of wavelength and the transfer function is given by:

$$P_{cross}(L) = P_{initial} sin^2\left(\frac{\pi \Delta n}{\lambda} L\right) \qquad \text{(Eq. 3.4)}$$

**(ii) Mach-Zender Interferometer Circuits:**

The individual photonic components – waveguides, grating couplers, directional couplers, y-splitters/combiners (50%/50%) are the basic building blocks of complex photonic circuits. A Mach-Zender circuit can be built in multiple ways – using directional couplers and connecting them with varying propagating length waveguides (by doing this we can also tune the circuit to provide any desired power ratios to the detector ports) connecting two y-splitters/combiners with two waveguides of same/varying path length. A Y-splitter functions by splitting the input power by half (into each waveguide) and can combine light (if I is the input power and E is the input electric field intensity, then the power through splits are I/2 each and the electric field intensity is E/$\sqrt{2}$ on each of the splits). It can also be termed as a multi-mode interferometer where odd and even modes interfere and result in a binary yes/no output in the resultant waveguide. There are ways by which the light mode in these waveguides can be manipulated 1. Use modulators 2. Induce a phase change in the source waveguide.

This light mode manipulation, allows the Mach-Zender interferometer be able to be customized and obtain a wide range of results like switching power completely from port to

another, get desired power split to the outputs (Ex. 50:50, 60:40 etc.), phase shift modulation etc.

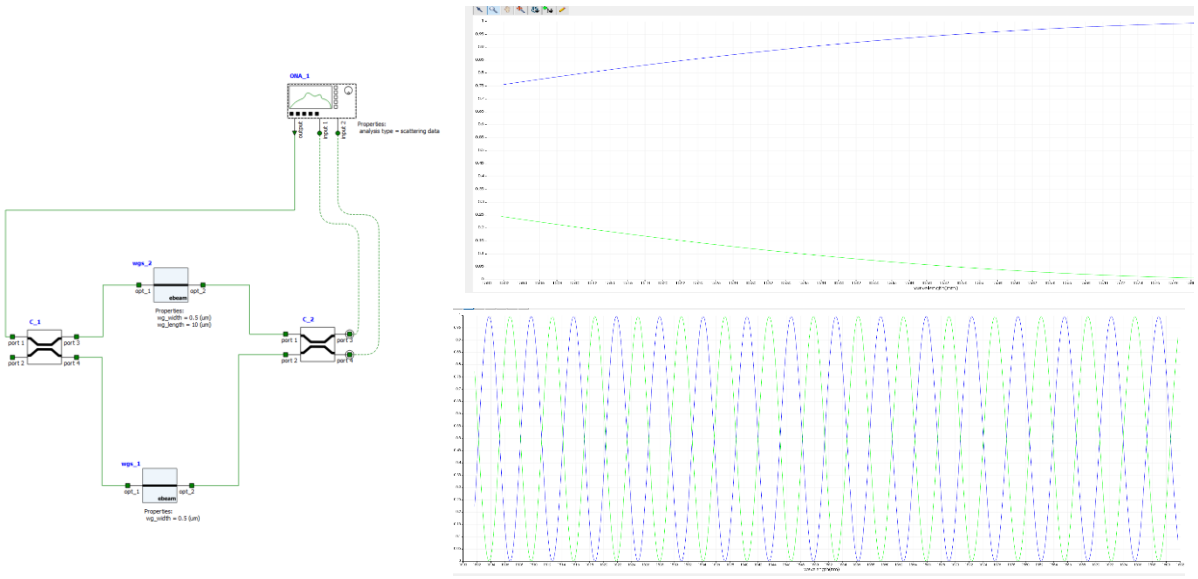

**Figure 3.8:** A nearly balanced MZI (ΔL = 1um) designed in interconnect to get a customized transmission split of 10:90 at 1550 nm; bottom plot – unbalanced

The transfer function of a Mach Zender Interferometer is:

$$I_{output} = I_{input}(1 + \cos(\beta \Delta L)) \qquad \text{(Eq. 3.5)}$$

From fig 3.8 bottom right plot, it is evident that the MZI has a cosine response and has a strong wavelength dependence for unbalanced circuits. Hence, depending on what percentage of transmission is needed, the wavelengths can be selected accordingly.

## 3.4 Ring Resonator Circuits:

Ring resonators are built by creating a waveguide loop and having it coupled to one input waveguide (single-bus configuration) or two waveguides (double-bus configuration). A ring resonator works like a directional coupler with 4 ports, except that the light is coupled into a ring with a circumference 2πR.

K is the cross transmission of a coupler

t is the straight input transmission of a coupler

Under ideal cases, the cross transmission 'k' is much smaller than the straight transmission 't'.

$|K|^2 + |t|^2 = 1$

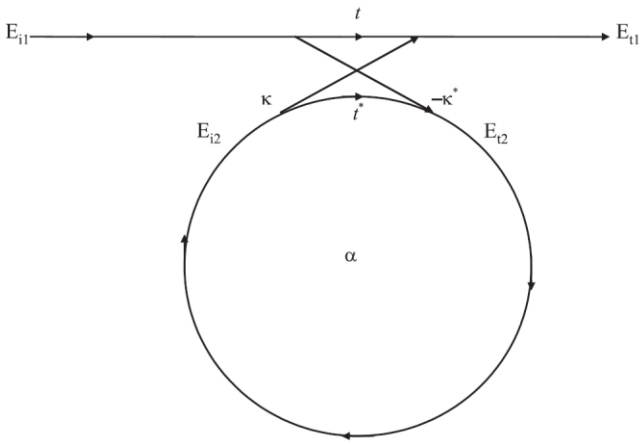


**Figure 3.9**: Ring resonator - single bus configuration [5]

The four ports can be labelled as $E_{i1}$, $E_{i2}$, $E_{t1}$, $E_{t2}$

$$\begin{pmatrix} E_{t1} \\ E_{t2} \end{pmatrix} = \begin{pmatrix} t & k \\ -k^* & t^* \end{pmatrix} \begin{pmatrix} E_{i1} \\ E_{i2} \end{pmatrix} \quad \text{(Eq. 3.6)}$$

$E_{t1} = tE_{i1} + kE_{i2}$ – electric field through the input waveguide

$E_{t2}$= -k$E_{i1}$ + t$E_{i2}$ – electric field that is coupled across the ring

For each trip inside the ring, the light will experience a phase delay and loss. Let α be the loss coefficient. The light is also travelling distance of L=2πR. The net loss is given by:

$$A = e^{-\alpha L} \quad \text{(Eq. 3.7)}$$

$E_{i2} = \sqrt{A}e^{i\beta L}E_{t2}$ – electric field through the ring (Eq. 3.8)

Substituting the values of $E_{i2}$ in the parent equations and solving for $E_{t2}$,

$$E_{t2} = \frac{-kE_{i1}}{1-t\sqrt{A}e^{i\beta L}} \quad \text{(Eq. 3.9)}$$

Substituting $E_{i2}$ and $E_{t2}$ in 1, we get

$$E_{t1} = \frac{t-t\sqrt{A}e^{i\beta L}}{1-t\sqrt{A}e^{i\beta L}}\ E_{i1} \quad \text{(Eq. 3.10)}$$

Converting the above "cross over and input" electric fields into power (I= $|E|^2$), the transmission equation becomes,

$$T = \left|\frac{t-e^{\frac{-\alpha L}{2}}e^{i\beta L}}{1-te^{\frac{-\alpha L}{2}}e^{i\beta L}}\right|^2 \quad \text{(Eq. 3.11)}$$

**Resonance Condition:**

When the ring resonator is said to be in a resonance condition, the propagating wavelength through the ring βL (β is the propagation constant = $\frac{2\pi n}{\lambda}$ and since it is moving a distance of 2πR, we multiply it by L) becomes an integral multiple of the circumference of the ring

$$\beta L = m2\pi \quad \text{(Eq. 3.12)}$$

$$2\pi R = \frac{m\lambda}{n} \quad \text{(Eq. 3.13)}$$

Substituting m=1 and $\beta L = 2\pi$, in Eqn. 3.11, the transfer function becomes:

$$T = \left| \frac{t - e^{\frac{-\alpha L}{2}}}{1 - te^{\frac{-\alpha L}{2}}} \right|^2 \quad \text{(Eq. 3.14)}$$

**Critical coupling condition:**

When t, the 'input waveguide' transmission is $e^{\frac{-\alpha L}{2}}$, the total transmission through the circuit becomes 0 (from Eq.2). This condition is called critical coupling (when the coupling loss is equal to the ring loss). During critical coupling, the ring loss is at a very low state, the light in the ring continues to increase in intensity. A small proportion of the light in the ring is lost to the input waveguide in the form of 'k'. When this happens, the incoming light destructively interferes with the light in the input waveguide and the total transmission at the end of the through input waveguide ($E_{t1}$) becomes 0. The light that is already in the ring eventually is lost to the evanescent field (this evanescent loss is in the case of a single bus ring resonator where there is no waveguide to carry over the 'drop' light from the ring).

In a lossless ring, the light coupling from the input waveguide goes through the ring, comes out as it is (except with a change in phase). This is a called an 'all pass' ring.

The important performance indicators for a ring resonator are the Q factor and the FSR.

$$FSR = \frac{\lambda^2}{Ln_g} \quad \text{(Eq. 3.15)}$$

$$Q = \frac{\pi Ln_g\sqrt{tA}}{Ln_g(1-tA)} \; or \; \frac{\lambda}{\Delta\lambda} \quad \text{(Eq. 3.16)}$$

Where $\Delta\lambda$ is the full width at half-maximum; higher the Q factor, better the ring performance

## 3.5 Mask Design

There are four levels used in the design process i.e. the waveguide, resistive metal heater and wiring, aluminum etch and contacts etch. All the levels in this quadrant mask are clear field. This was done considering the feasibility of lift-off metal processing and the advantages of using a negative resist (etch masking and NR9 1500PY resist serves dual purpose – negative tone and lift-off). The maximum writable area on the mask is 22000 $\mu m^2$ (on-wafer 5x reduced dimensions) and this area is split into 4 quadrants of 11000 µm x 11000 µm for each of the 4 layers.

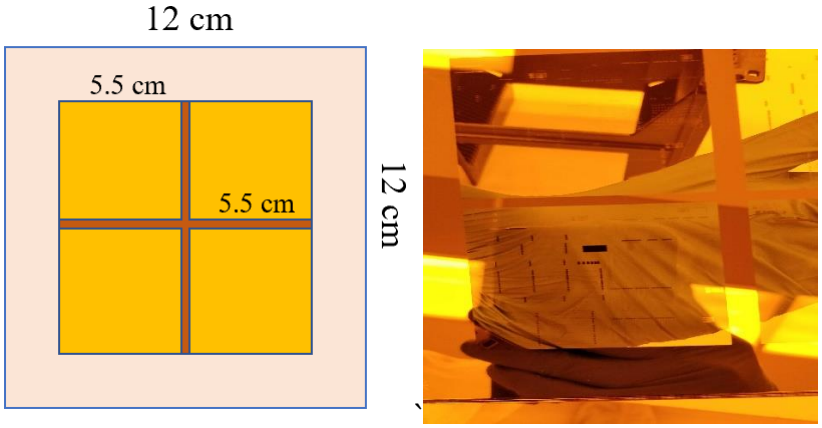


**Figure 3.10**: Physical mask layout (5.5 cm / 5 = 1.1 cm =11 mm= 11000 µm)

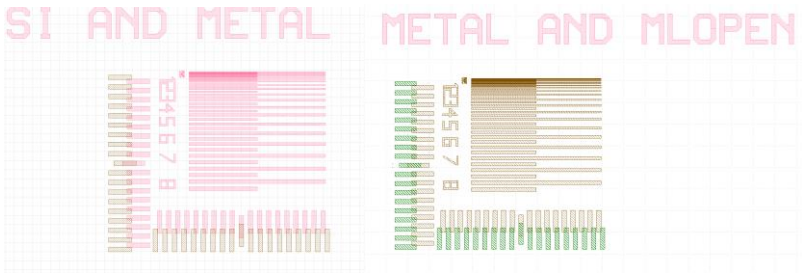


**Figure 3.11:** Alignment overlay

Alignment overlay structures shown in Fig. 3.11 and verniers need to be included for all 4 layers to verify the alignment after each exposure level. Since resistive metal stacks are being used, TLM (Transmission Line Measurement) structures were designed to verify the contact resistance.

The grating couplers used for design have a pitch of 1.25 μm and are separated by 125 μm from each other (the fibers in the array have a pitch of 125 μm). The circuit variations were introduced by modifying the cell scripts for respective components. For example, variations in ring resonators having 0.4, 0.45, 0.5, 0.6 μm gaps were done in a single bus resonator circuit. Similarly, variations in grating coupler duty cycles were also added to determine the best coupler design for vertical coupling and all the circuits were designed to be TM polarized. In addition to this, to account for the etch width loss in fabrication (hard mask erosion), passive circuits with 600 nm width were designed to calculate how much of a mask bias is required while designing the photonic circuits for future fab work at RIT.

The heaters were designed according to the geometry of the passive components they served.

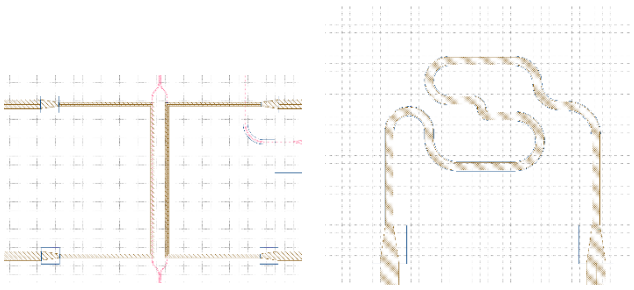

**Figure 3.12**: MZI heater (left) Ring heater (right)

The wires extending from the main heater were designed to be 5 μm wide and 1000 μm long connecting to the contact pads of 50 μm x 50 μm. The total resistive ring heater design can be split in to 3 parts (i) Ti ring heater (ii) Ti/Al wire (iii) Ti/Al contact pads. This can be seen in Fig. 3.13.

Contact resistance of any metal contact should be sufficiently low so that the applied power is completely transferred into the circuit without much loss. The measured resistance was ~ 3 mΩ and was done with TLM (Transmission Line Measurement) structures having a titanium thickness of 50 nm covered by aluminum 200 nm. Resistance calculations were done using the standard resistivity values of Ti = $4.20 \times 10^{-7}$ Ωm and Al = $2.68 \times 10^{-8}$ Ωm for different sections of the ring heater design (pads + wire + ring). A total of 0.03 Ω was calculated for the current carrying heater wire where there are two metals in parallel ($1/R_1 + 1/R_2$). In the ring heater region, Ti heater width was reduced to 2 μm and runs for a total of ~100 μm along the circumference of the passive ring resonator, giving a total resistance of 420 Ω. The dimensions for design and calculations can be seen in Fig. 3.13.

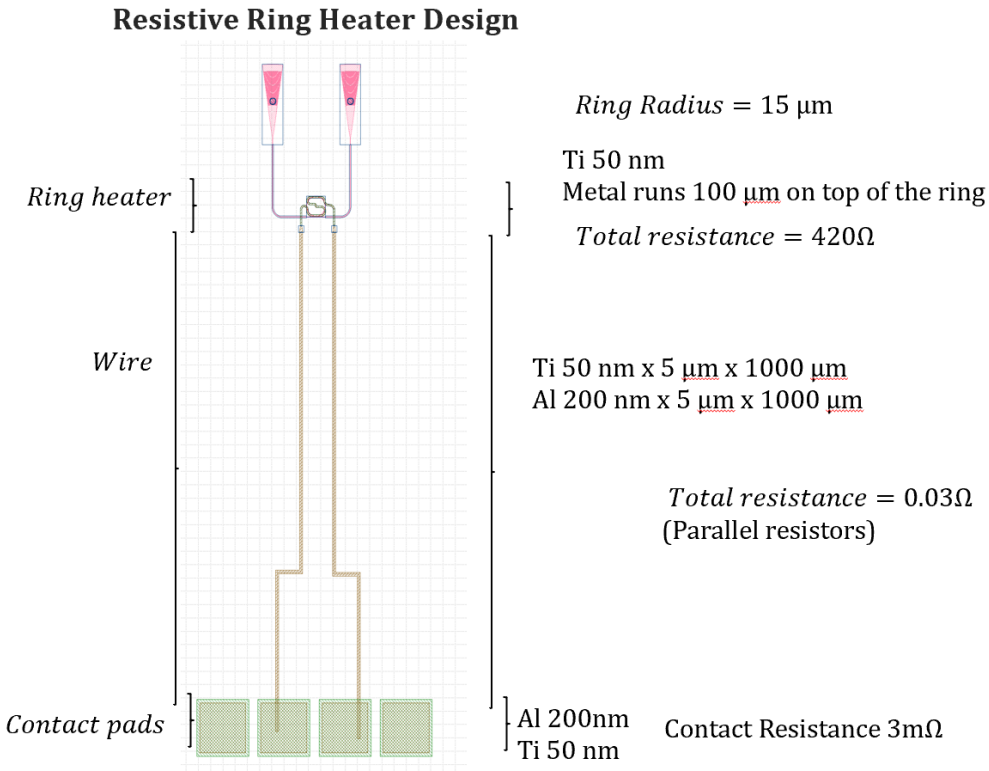


**Figure 3.13:** 2 µm Ti ring heater with 5 um Ti/Al wires terminating in 50 µm x 50 µm Ti/Al contact pads

# IV. Fabrication Process

## 4.1 Processing Fundamentals:

This section will cover the important background theory behind most of the processing techniques that are used with respect to the requirements this thesis and in the order in which they are used.

**Plasma Enhanced Chemical Vapor Deposition (PECVD): Oxide**

A plasma generated CVD system can be characterized by the presence of a RF generator, matching network, vacuum systems, flow and thermal controllers among other components. The process can be defined as the formation of a thin film with the help of various gas sources ionized in a plasma that react to create the thin film on the substrate. PECVD reactors use RF power sources instead of just thermal energy to strike the plasma and carry out the gas phase chemical reactions. Thus, faster deposition rates are achieved compared to thermal processes where the substrate usually heats up to a very high temperature to transfer energy to the reactant species. The electrons that are created in the low pressure – high vacuum plasma region gain energy from the applied RF field and collide with the gas molecules that triggers a series of dissociation and ionization reactions. The resultant radicals are then adsorbed on to the wafer surface. The stoichiometry of the gas precursors, RF source, pressure, position of the shower heads, chamber contamination etc. play a major role in the deposition and quality of the resultant film.

$$si(OC_2H_5) \rightarrow SiO_2 + 4C_2H_4 + 2H_2O \qquad (5.1)$$

In this thesis, a single wafer PECVD cluster tool is used in the deposition of $SiO_2$ formed from the decomposition of Tetra Ethyl Ortho Silicate (TEOS) for cladding the waveguides. Although there are other methods to deposit $SiO_2$, decomposing TEOS using PECVD is quicker and consumes less of the thermal budget. The process can be easily engineered to produce high quality and conformal oxide films.

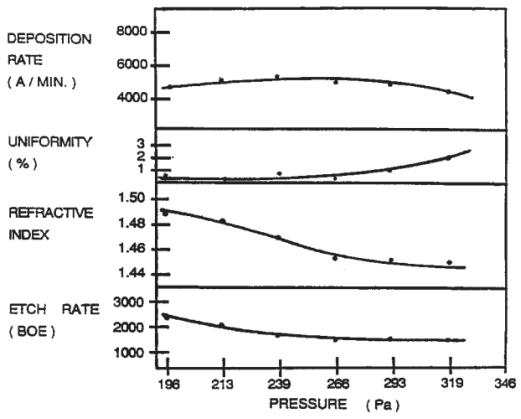


**Figure 4.1:** PECVD oxide process plot [6]

According to Fig. 4.1, the refractive index is tightly controlled between 1.49 and 1.45 for PECVD oxide films (for silicon the refractive index is 3.45). This optimal difference in the refractive index between the waveguide and cladding allows total internal reflection and confines the light to stay within the waveguide and lower bend radius.

**Photolithography:**

One of the major requirements of photonic circuit fabrication is the need to create a reliable and a repeatable process to reach the target lithographic resolution with the given stepper specifications. With multiple lithographic levels, qualification of each layer becomes a bit complicated compared to earlier levels. Although doing FEM analysis of individual layers on

bare silicon wafers provide the required exposure dose and focus, when it comes to the entire stack, the stack reflectivity, absorption coefficients, topographical issues like surface roughness, conformal coatings all come into play. Hence, it is of utmost importance to start with good quality wafers with minimal contamination and little to no processing.

In conventional photolithography, the standard processing steps are de-hydration bake, resist coating, soft bake, exposure, post-exposure bake, develop and hard bake. The photoresist is usually chemically amplified i.e. when the positive resist is exposed to light, the photons react with the chemical components in the resist and forms a photoproduct which triggers a series of 'amplification' reactions and makes the photoresist soluble to the developer solution. Baking is generally done to provide additional thermal energy to increase the rate of these reactions (in the post-coat soft bake, the casting solvents are removed). The post exposure bakes are done to get crisp sidewall profiles by reducing the standing wave effects. Post development bakes are done to harden the resist and make it more etch resistant to favor subsequent processing steps. In the case of a negative resist, the exposed regions become insoluble to the developer solution and the post exposure bake (mostly called as the image-reversal bake) plays an important role in crosslinking the exposed region.

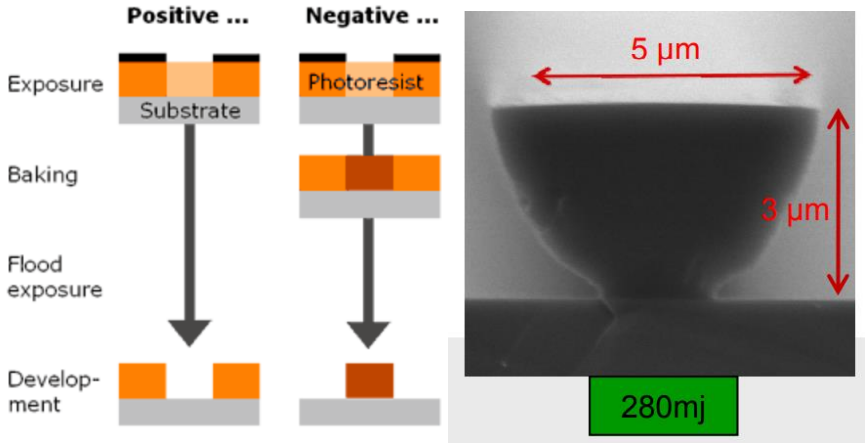


**Figure 4.2:** Positive and Negative resist behavior(left), undercut in a negative lift-off resist (right) [7]

Perfect anisotropic etching with good selectivity of the target material with the masking material and side wall profiles are needed for successful pattern transfer after lithography. In this thesis, pattern transfers are done using the Reactive Ion Etching mechanism.

**Dry Etch Processing:**

Dry etching process takes precedence over wet etching as anisotropy is a critical requirement for pattern transfer after lithography. In addition, etch selectivity and uniformity should be considerably good with minimal masking erosion for an optimal dry etch process. Reactive Ion Etching is a combination of a glow discharge sputter and chemical based etch process. Fig. 4.3 shows the basic sequence of plasma etch processing.

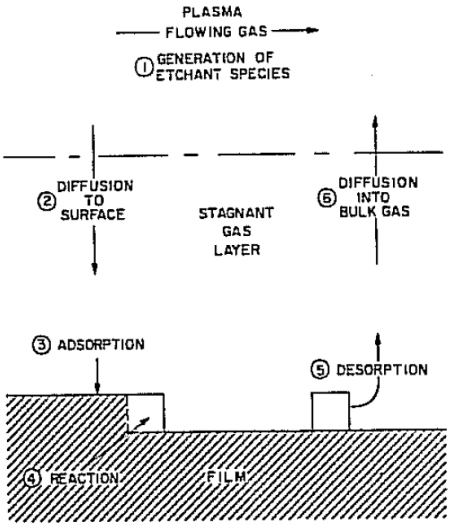


**Figure 4.3:** Dry etching sequence [8]

Electrons, positive ions and free radicals are the three main components (etchant species) in a glow discharge/plasma. These are generated by the striking the etchant gases supplied in controlled proportions using the flow controllers with an RF source. The positive ions are ideally heavier than the negatively charged electrons and the radicals neutral without any charge, readily available for reaction which are responsible for the etching mechanism. Process variables like pressure, RF power, distance of separation between the wafer and the upper electrode (varies with different systems), gas flow proportions, etch time are responsible for desired anisotropic etch profiles with good selectivity. The two main types of RIE are capacitively coupled and Inductively coupled plasma etching. The major difference between these two modes is the plasma density. The CCP has lower plasma density and the electrode that is not connected to the RF source is grounded. The etchant species undergo a series of excitation, ionization, dissociation and attachment releasing a large quantity of free electrons which makes the gas electrically conductive. This process is accompanied by the release of light energy and hence the glow. The ionization efficiency (IE) (the ratio of the

number of ions generated by the electrons and protons in the plasma) of a CCP plasma is ~ $10^{-7}$ and is lower compared to a high density Inductively coupled plasma (IE is ~$10^{-3}$). In high density plasma, the ion bombardment energies are relatively lower, and this helps in reducing physical sputter damage to the surface of the wafer. While lower ion energies reduce the anisotropy and etch rate, operating at a lower pressure can compensate and restore the same.

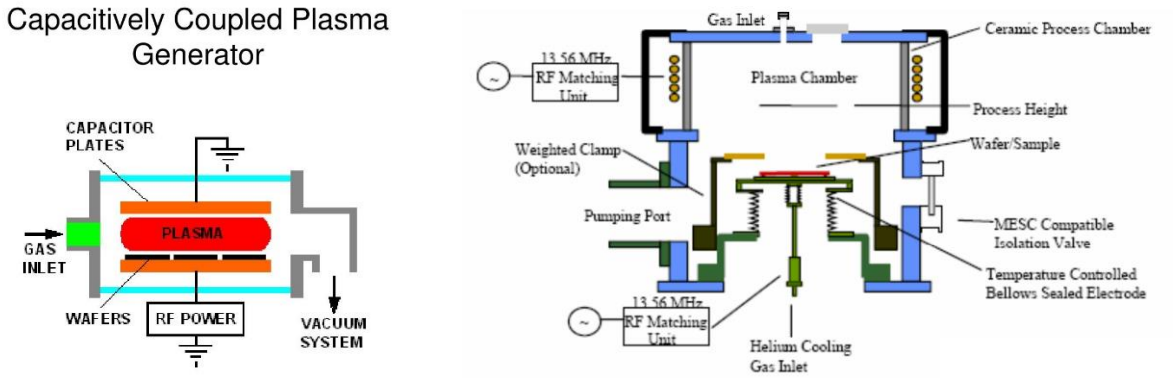


**Figure 4.4**: CCP RIE vs ICP [9]

**Spin on Carbon – hard mask material**

Masking layers for dry etch processes are a key component and should have good etch resistance. In this thesis, among other materials (cured photoresist, CVD oxide) that were chosen to mask the silicon before the waveguide etch, carbon (IM HM140 spin-on) showed excellent resilience to etch. The selectivity of this material is 1:9 to silicon [10]. The uniformity and etch resistant properties however depend on the dispense ramps, final spin speeds and the final hard bake. With the current established process in this thesis (section 4.2), a high die yield percentage per wafer of ~80% was made possible (i.e. out of the 36 dies, 30 were tested to work successfully with 0.4 µm ring gaps resolved successfully).

The IM HM 140 is primarily made up of cyclohexane 90% which has a chemical formula $C_6H_{12}$. The other ingredient listed in the SDS is a standard novolac polymer meant for crosslinking. The properties of SOC vary with temperature (baking conditions) and is proven to successfully transfer 20 nm patterns [10].

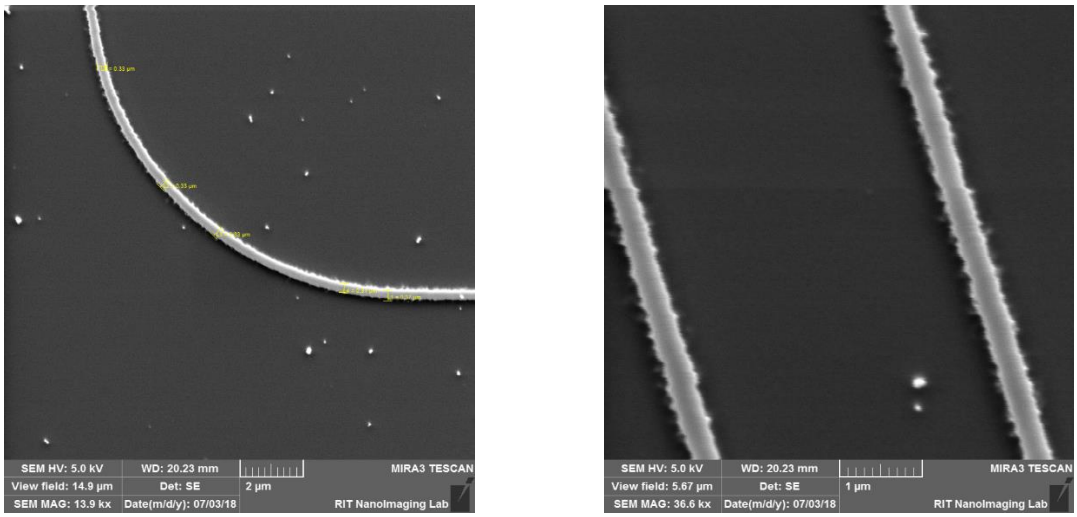


**Figure 4.5:** SEM images of silicon waveguides - erosion effects and thinned waveguides without hardmask material

**Cladding:**

After the silicon etch, the waveguides need to be clad with a suitable material that allows maximum total internal reflection with minimal scattering loss. Two materials have been explored for cladding the waveguides, photoresist and $SiO_2$. Photoresist with an average refractive index of 1.70 and an extinction coefficient of 0.02 for general AZ positive tone resists at 365 nm i-line. $SiO_2$ with an average refractive index of 1.4 which is effectively glass formed from the PECVD decomposition of TEOS. Cladding with $SiO_2$ allows better light coupling to the optical fiber array in addition to protecting the circuits from external contamination. The only problem that might be faced while using $SiO_2$ for cladding is the conformity (seen in Fig. 4.6) to the waveguides and the buried oxide (bottom cladding).

Photoresist is more viscous compared to a chemical vapor deposited TEOS layer and might conform well to the waveguides. Any slight variation in the anisotropic silicon etching/hardmask erosion problems/ any sort of undercut to the waveguides will cause coupling problems.

For the current process, there will be two cladding oxide depositions (explained in section 4.2). One is right after the Si waveguide etch (to isolate the waveguides from the heaters) and the second deposition is after the metal deposition so that the complete package is now enclosed with enough $SiO_2$ for light coupling.

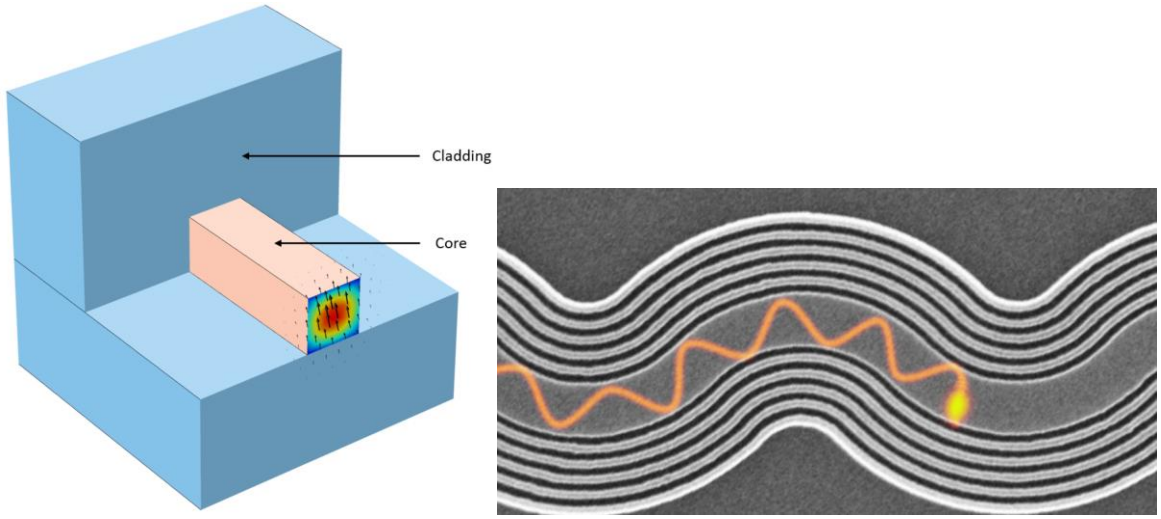


**Figure 4.6:** Cladding and representation of a conformal deposition to waveguide [11]

## 4.2 Fabrication Process Flow

The process flow involves the integration of two major phases. The first part is the fabrication of passive photonic components and the second phase involves the active heater component integration. The motive is to develop a reliable process flow for photonic components fabrication with modulation capabilities in an academic clean room environment. Each part of this chapter will involve the investigation of processing anomalies that were encountered over the course of this thesis.

**Phase I – Passive Photonic Circuits fabrication**

**Level 1: a- Si waveguide etch**

Prime grade silicon n-type 100 oriented with a standard thickness of 650 – 700 μm forms the base layer of the Pseudo SOI as industry grade SOI wafers are expensive. Plasma Enhanced Chemical Vapor Deposition (PECVD) of 2 μm TEOS (Tetra Ethyl Ortho Silicate) forms the buried oxide layer which later becomes the bottom cladding for the waveguides. The recipe for PECVD oxide deposition can be found in table 4.2. A 220 nm thick amorphous silicon, which is proven to exhibit better non-linear effects compared to crystalline silicon, is deposited using PECVD at Cornell Nanoscale Facility (CNF) as RIT's fabrication facility is not equipped with an a-Si deposition tool.

The a-Si wafer now can be treated as a regular silicon wafer. After the initial RCA clean, a dehydration bake is done at 110˚C to get rid of the surface moisture content.

Spin on carbon (IM HM 140), BARC (ICON 7) and Photoresist (AZ MiR 701) are now coated on the wafer using recipes in table 4.1. and the wafer is now made ready for i-line exposure.

It is important to do an exposure meander on the actual wafer stack at all lithography levels. Each film will have its reflectivity and transmission properties. After a proper Focus and Exposure matrix on the waveguide layer, it was found that a dose of 170 mJ/cm$^2$ with a focus offset of 0.1 was able to resolve a 300 nm space in between two 500 nm lines. The exposure is followed by an immediate Post Exposure Bake of 110˚C of the top photoresist layer which will provide a crisp the side wall profile and reduce standing waves in the resist. The wafer is now developed to remove the exposed photoresist and this process is done for 53 seconds. A Post Development hard bake (PDB) at 140˚C is required to make photoresist more resistant to the upcoming etch process.

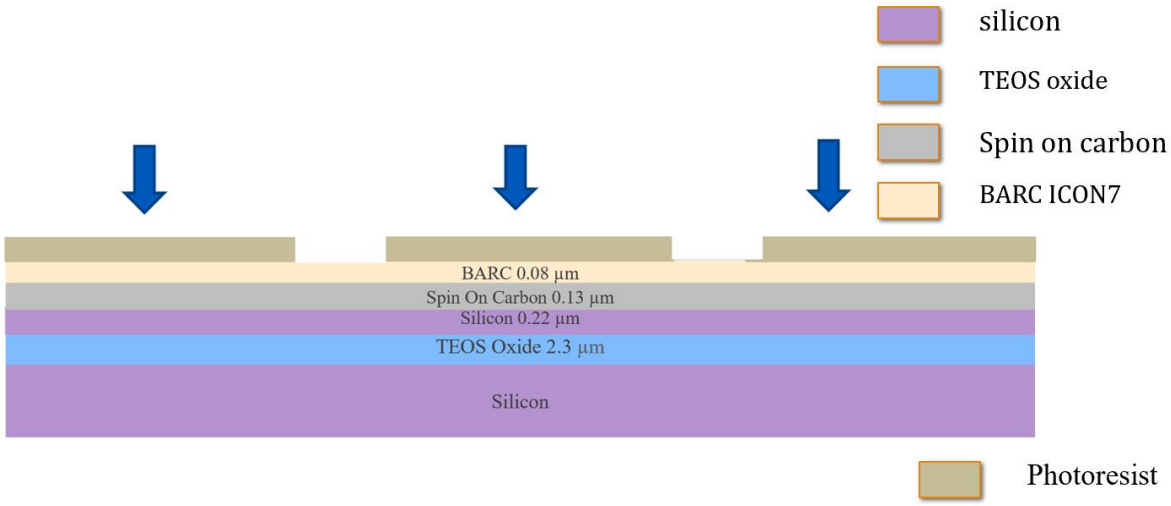


**Figure 4.7:** Process cross section - waveguide patterning

The patterned waveguides are now protected by SOC, BARC and photoresist. The field region which is now covered by just BARC and SOC underneath, needs an RIE for an anisotropic pattern transfer with good side wall profile and reduced mask erosion. The recipe for this process can be found in table 5.3. This is followed by the shallow 220 nm silicon etch done

in a DRIE (Deep Reactive Ion Etching) system operating in ICP mode. The wafer is now de-scummed in an $O_2$ plasma to remove residual resist leaving just the waveguides.

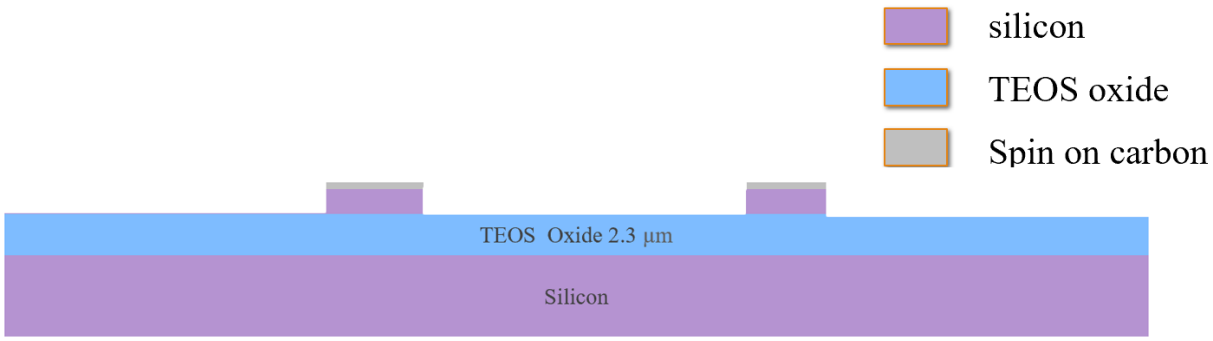


**Figure 4.8:** Process cross section - after silicon etch

**Table 4.1:** Coating Recipes

| Material | Initial Ramp | Spin Out | Soft Bake |
|---|---|---|---|
| Spin on Carbon | 3s to reach 500 RPM, 5s | 10s to reach 2500 RPM, 60s | 300˚C 180s |
| ICON7 | 800 RPM,1s | 1500 RPM, 30s | 170 ˚C 60s |
| Diluted AZ MiR 701 | 800 RPM,1s | 3000 RPM,30s | 95 ˚C 60s |

**Table 4.2:** PECVD $SiO_2$ Deposition Recipe

| | |
|---|---|
| **Tool Name/Process** | P-5000 Chamber A - PECVD |
| **Masking/Protection Film** | NA |
| **Gas Names & Flows (in SCCMs)** | TEOS 400, $O_2$ 285, He 405 |
| **Operating Pressure** | 9 Torr |
| **Operating Power** | 285W |
| **Deposition Rate** | 0.59 µm/ min |
| **Recipe Name** | 1 µm TEOS LS |

**Table 4.3:** Etching Recipes

| | | |
|---|---|---|
| **Tool Name/Process** | Trion Minilock RIE | STS DRIE – ICP Mode |
| **Masking/Protection Film** | Photoresist | Carbon |
| **Etching layer** | BARC and Spin on Carbon | a-Silicon |
| **Gas Names & Flows (in SCCMs)** | $O_2$ 10 | $C_4F_8$ 60, $SF_6$ 20, $O_2$ 2, Ar 40 |
| **Operating Pressure** | 50 mT | 20 mT |
| **Operating Power** | 100W | 725W |
| **Etch Time** | 75 seconds | 8 mins (loading effect) |
| **Recipe Name** | Manual | Venky |

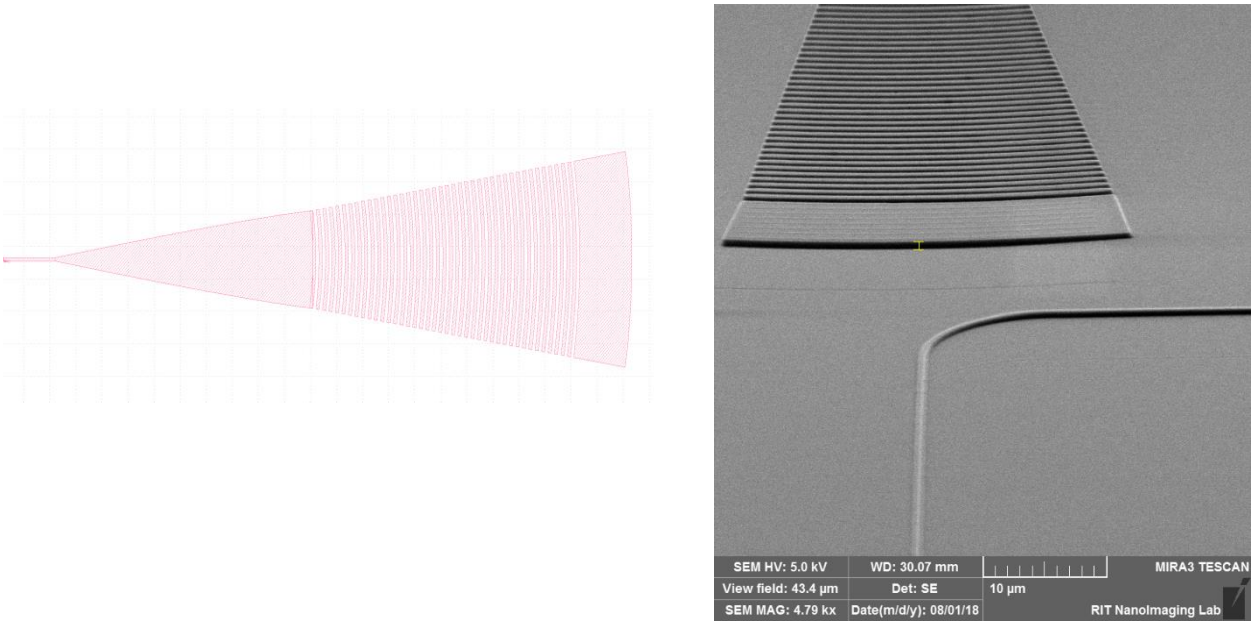


**Figure 4.9**: Grating coupler design (left) Vs Fabricated grating coupler (right)) - after Si etch

**Cladding Deposition:**

The etched waveguides now need to be clad with $SiO_2$. The PECVD deposition recipe in table 5.2 is used to deposit 1 µm thick oxide on the silicon. The passive photonic circuits fabrication process is now complete and is ready for optical probing.

**Phase II – Active heater component fabrication**

**Lithography Level 2:**

The cladding also acts as the separation between the silicon waveguide core and the metal layer (a thick oxide cladding prevents the metal from absorbing the light that passes through the waveguides). In this thesis, lift-off process is followed for the metal layer deposition (lift-off process eliminates the need for metal etch). A negative mask design is ideal for a good lift off as it is convenient to have a greater proportion of the metal to be removed rather than

lifting off the minority portion. A clear field mask design for the heater layer (shown in Fig. 4.12), will allow the metal to lift off in the field region leaving behind the patterned metal heaters on the photonic circuits.

For this process, Futurex NR9 1500PY - a dual purpose 'negative lift-off' photoresist is used. The spin speeds and the soft bake temperature can be seen in table 4.4. After the coat, an exposure dose of 90 mJ/cm$^2$ was found to clear the photoresist. After the exposure a 110˚C post exposure bake and a total of 18 secs develop on the develop track was found to clear the unexposed photoresist. Post development hard bake is usually skipped for lift-off resist processing to prevent resist crosslinking and might prevent it from lifting off properly.

Table 4.4: Coat Recipe for Futurex NR9 1500PY photoresist

| Material | Initial Ramp | Spin Out | Soft Bake |
|---|---|---|---|
| Futurex NR9 1500PY | 100RPM, 1s | 2900 RPM, 40s | 110˚C |

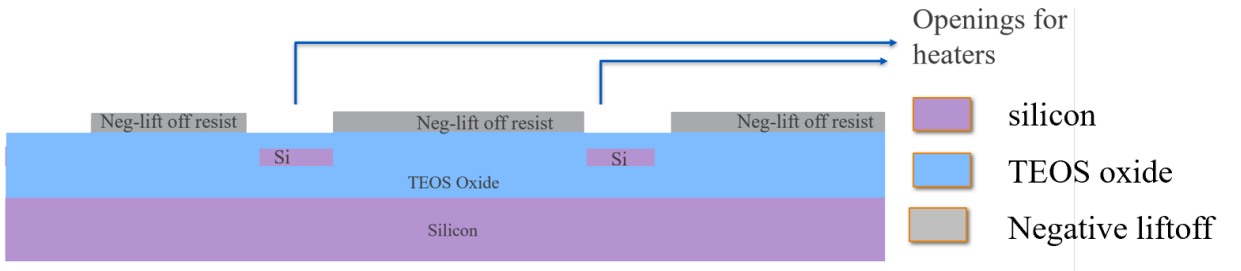


**Figure 4.10:** Process cross section - heaters definition

**Metal Sputter:**

The metal sputter process was developed to minimize the deposition rate (reducing stress) and to get good uniformity. An overnight pump down will allow the chamber to reach a base pressure in the order of $10^{-7}$ mT (low pressure, high vacuum). Recipe in table 4.5 is followed for the Ti/Al stack sputter. Titanium can readily oxidize and form $TiO_2$ which is an insulating layer, when exposed to the atmosphere. For this reason, it is important to have the metals sputtered without breaking vacuum. An interval of 5 minutes is given after the Ti sputter before switching the power to the Al sputter target.

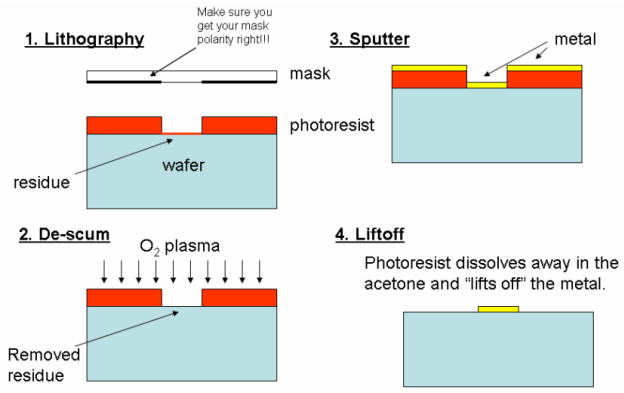


**Figure 4.11**: Lift-off processing

**Table 4.5:** Metal sputter recipes

| Parameters | Titanium | Aluminum |
|---|---|---|
| Power | 450W | 1000W |
| Metal Target Size | 4” | 8” |
| Base Pressure | 2.2 x $10^{-7}$ mT | 2.2 x $10^{-7}$ mT |
| Chamber Pressure | 5 mT | 5 mT |
| Sputter gas | Ar 20 SCCMs | Ar 20 SCCMs |
| Deposition time | 620 seconds | 1000 seconds |
| Thickness | 50 nm | 150 nm |

**Lift-off Process:**

Metal lift off in done on an ultrasonic bench using NMP (1-methy 2-pyrolidone). Heating up the bath to 40˚C with sonication fastens the process and removes the underlying photoresist along with the metal completely after about 30 minutes.

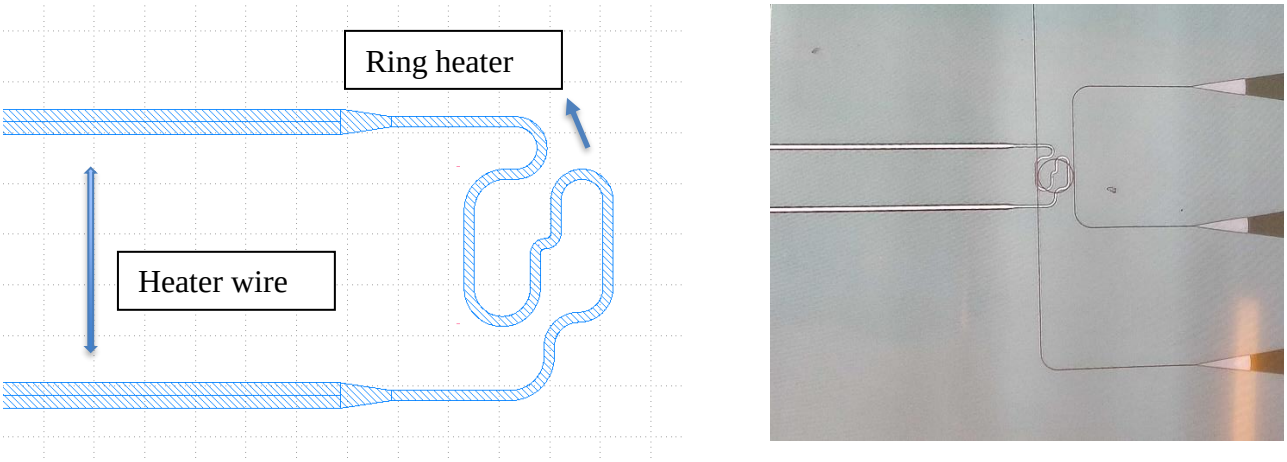


**Figure 4.12:** Ring heater design (left), ring heater on a double bus ring resonator (right)

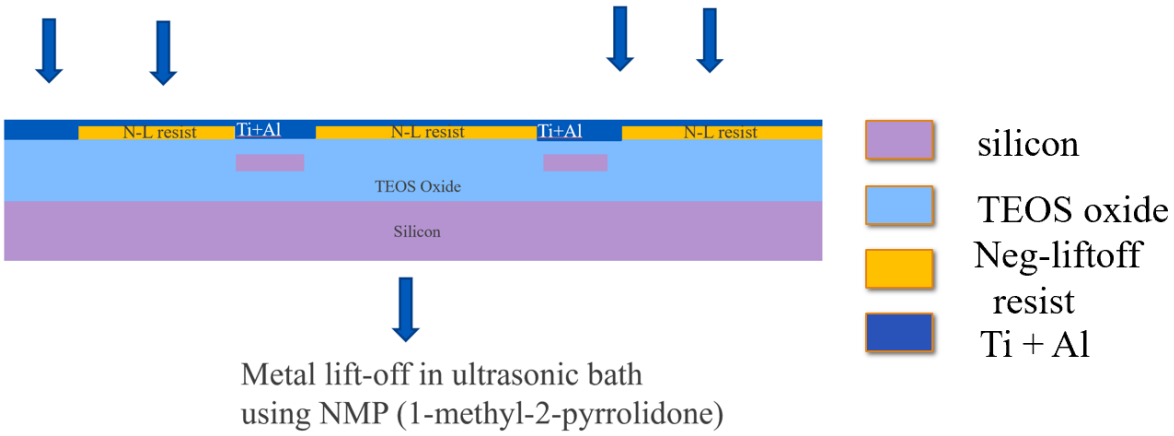


**Figure 4.13:** Process cross section - metal deposition and lift-off

**Level 3: Lithography and Aluminum etch**

The design was to create a low resistance path through the heater wire by having two metals in parallel so that the maximum proportion of the supplied power is transferred to the ring heater which has the high resistive metal (titanium).

For patterning the aluminum etch holes, a clear field mask design with negative photoresist processing was followed similar to the previous heater layer. Coat recipe in table was used and an exposure dose of 110 mJ/cm2 was found to resolve features as low as 1 µm. It was also noted that the exposure dose to get best resolution varied for different lithography layers (stack reflectivity and absorption effects).

After patterning the holes, a 16:1:1:2 Acetic acid+ phosphoric acid+ nitric acid mixture bath (the standard aluminum etch bath in RIT SMFL) was used to etch the aluminum. An etch test run prior to the actual run, gave a 50 nm/30 secs rate for the aluminum etch which was heated to 50 ˚C. So, including 10 seconds over etch, a total of 1 min and 40 seconds was set

on the timer for the etch process, knowing that the mixture will not etch the titanium [2]. The wafer was then set up for standard SRD (Spin Rinse Dry).

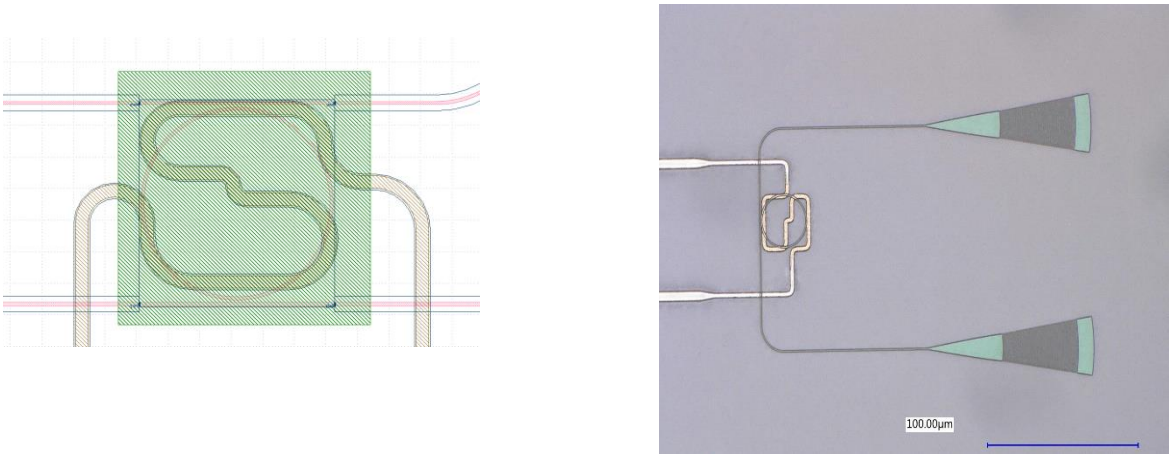


**Figure 4.14:** Window for aluminum etch (left), after aluminum etch (right) (note the color difference after etching)

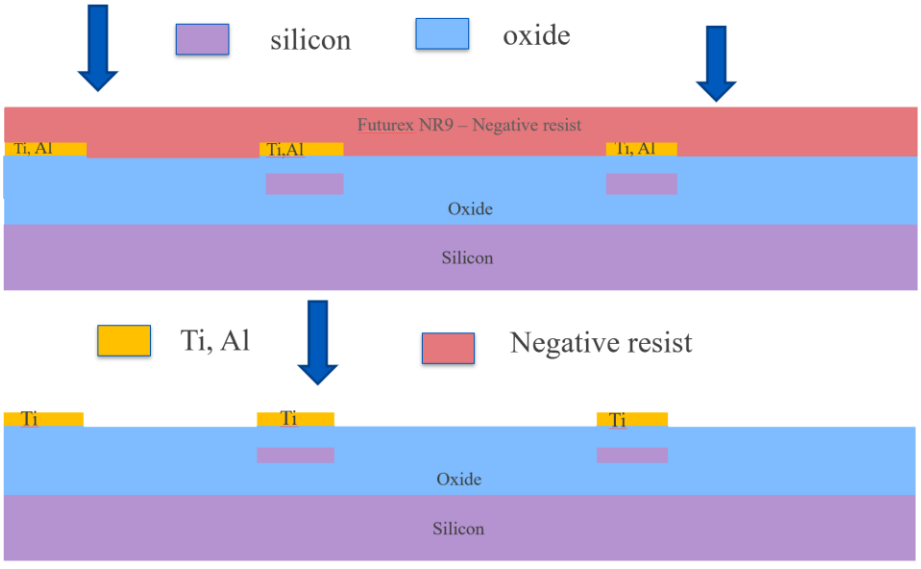


**Figure 4.15:** Process cross section - Aluminum etch

**Level 4: Lithography and contact pad oxide etch**

Recipe in table 4.2 is followed for a 200 nm oxide deposition. Patterning for contact holes also involve negative resist processing similar to the previous layers. A dose of 120 mJ/cm$^2$ was found to give the best resolution for this layer.

After patterning, a 16:2:2 Pad oxide etch (Ammonium Fluoride, Phosphoric Acid, Glycol and Surfactants) chemistry was used to etch the oxide in the openings. The etch rate measured earlier was approximately 150 nm/60 secs and the wafer was allowed to sit inside the bath for a total of 1 minute 30 seconds. The wafer boat was taken to spin rinse dry after the etch.

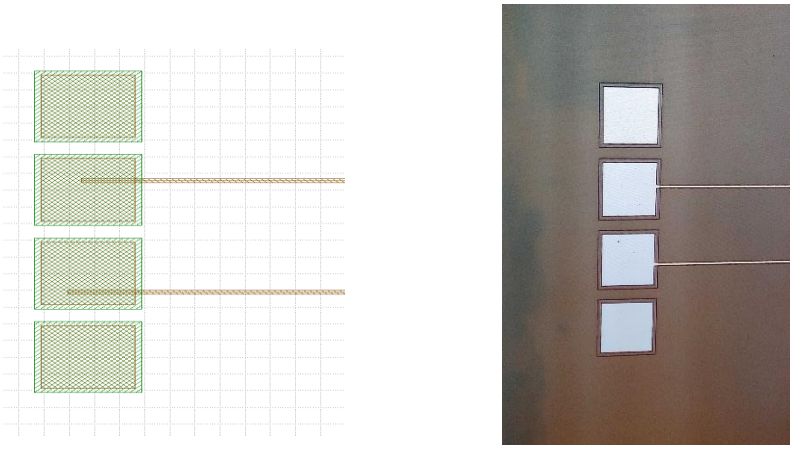

**Figure 4.16:** Openings for contact pads design (left), after oxide etch in the openings (right)

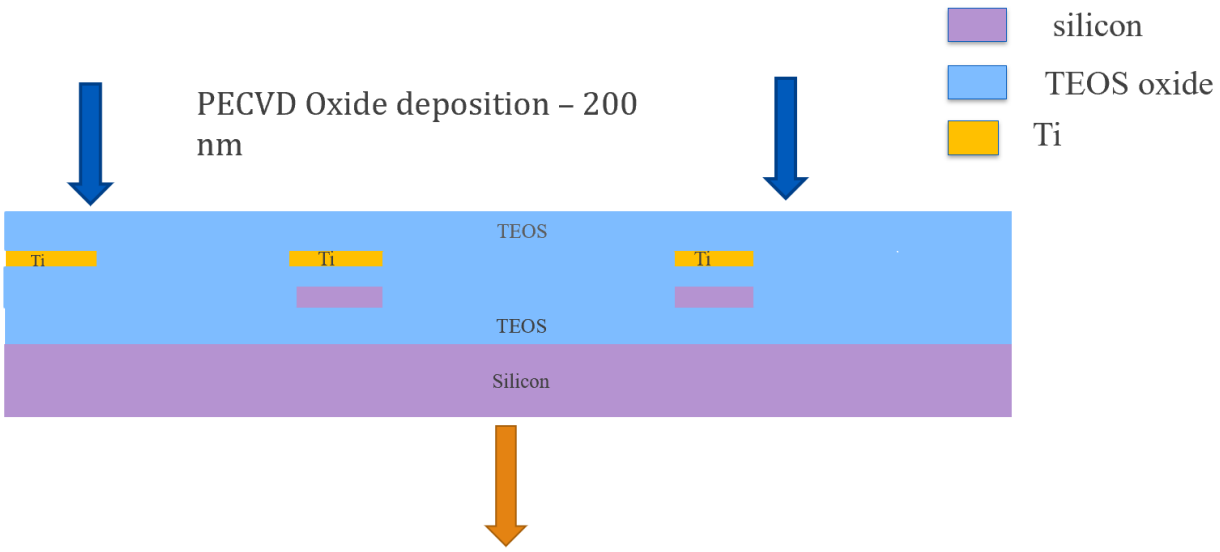


**Figure 4.17:** Process cross section - pad oxide etch

# V. Testing

## 5.1 Testing Setup

The fully fabricated photonic wafer was tested using the Maple leaf photonic probing station located at the RIT center for photonic communications. This testing set up comes with the flexibility to switch between vertical and edge coupling together with the electrical probing station (power supply). This station is also capable of operating in fully automatic and semi-automatic mode. The optical 4-fiber array was TM polarized and spacing between the individual fibers in 127 µm. The laser source is a keysight 8164B tunable laser (ECL) with a set power of 6 dBm into the singe mode fiber array with input in fiber 2 and other 3 fibers are used for detecting the output power coming out from the circuit. The fiber array was kept inclined at a 30˚ angle to get good coupling and the wavelength was swept from 1500 to 1600 nm.

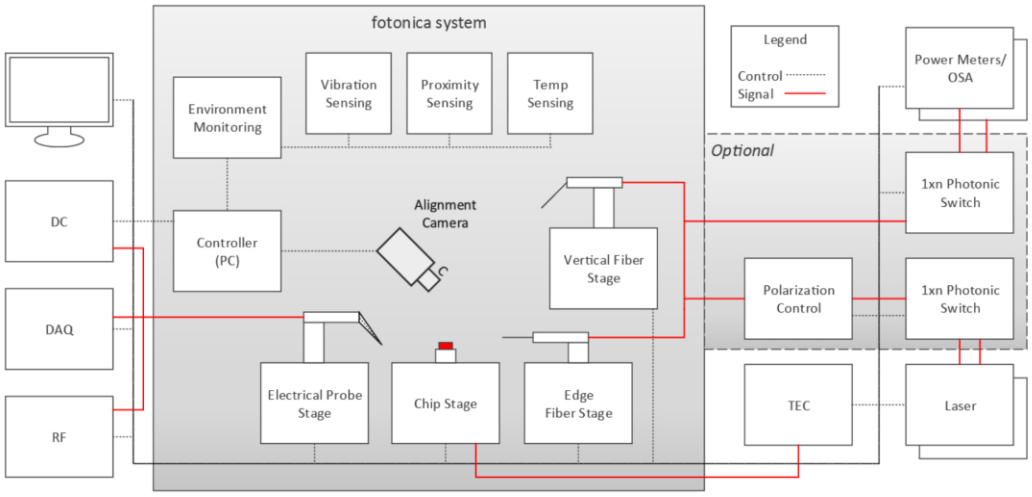


**Figure 5.1**: Optical and electrical probing station [12]

Academic wafer fabrication and testing is prone to extreme loss conditions which include wafer handling and transport, contamination, use of a-Si waveguides instead of crystalline silicon (standard SOI) inefficient design, improper input light polarization, larger bends, fabrication variation, unpolished fiber array and the height at which the fiber array is set for coupling onto the grating couplers (coupling loss can very at every manual circuit testing step). Even though a -3 dB waveguide propagation loss is expected by default, the circuits tested in this thesis have varying losses from a low -30 dBm to a high of -50 dBm. The primary motive of this thesis was to develop a reliable and repeatable process for active and passive photonic circuits fabrication. This process can now be engineered and customized to work better for future photonics research at RIT and for the photonic integrated circuit course.

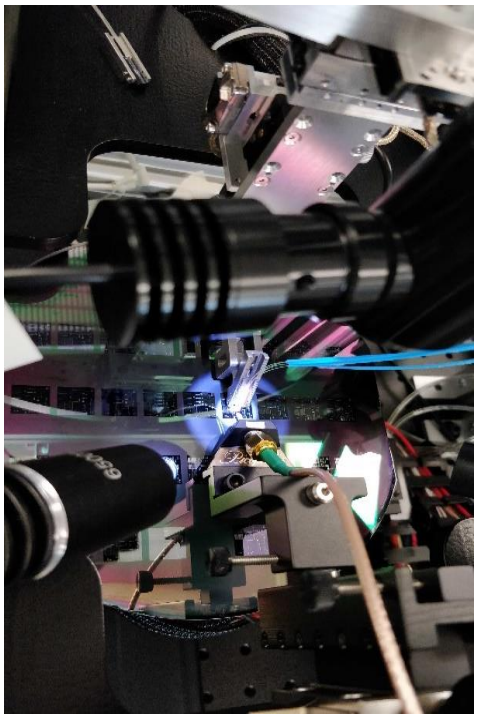

**Figure 5.2:** Photograph taken during testing

## 5.2 Testing Sequence

The station is setup with the fiber array to get vertical coupling on to the grating couplers and is mounted at a 30˚ angle on the stage. All the mechanical stage movements are executed using commands in the fotonica software that is connected to the testing system. The laser power, wavelength sweep, electrical probe sweep, fine alignment etc. can be configured and setup for an automatic sweep of the entire chip. In this thesis, manual testing/ individual probing is carried out as the main circuits of interest are the ring resonators and few other MZIs (both active and passive). The wafer is loaded onto the station stage and is kept in place with vacuum. The alignment camera is setup to get a zoomed in view of the circuits as shown in Fig. 5.3. The fiber array can now be controlled in the x, y and z directions to locate circuits for probing. A polarization paddle (a device capable of rotating the light) is connected in-between the laser supply and the fiber array probe. This polarization paddle ensures that the incoming light is TM polarized and block TE light modes. Since the circuits were designed to support only TM modes, without proper TM polarization setup, an extra -8 dBm loss was observed on every circuit response.

The electrical probe station is now mounted straight opposite (180˚) from the fiber array and is screwed down to avoid movement. The probe tips can be maneuvered minimally in the x, y and z direction to align with the circuit's probe pads which are separated by 100 μm. The probe tips are made of Nickel.

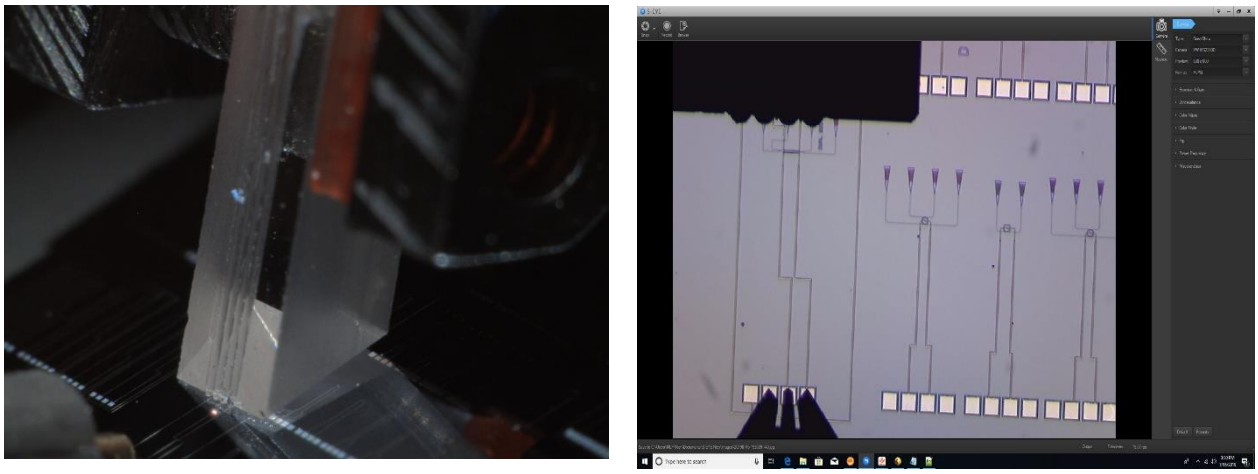

**Figure 5.3:** Photographs taken during testing

## 5.3 Interpretation of Power vs Wavelength Plot (Data Analysis)

In this section, the thermo-optic response of a double bus ring resonator circuit (add-drop configuration) is analyzed. As mentioned earlier in this thesis, a ring resonator has a combined working principle of a Mach-zender interferometer circuit and a bent waveguide. While the working is explained in chapter 3, this section will be focused on analyzing transmission/response plots from the testing circuits which were fabricated at RIT. A general power/response plot of a ring resonator circuit will provide details on the following (i) the total power loss through the circuit (ii) extinction of the circuit (iii) coupling efficiency of the ring (under-coupled or over coupled) (iv) transmission through the ring (v) loss in the ring (vi) Free Spectral Range (FSR). In addition to this, the quality factor (Q) of the ring was also extracted as a measure of the ring efficiency.

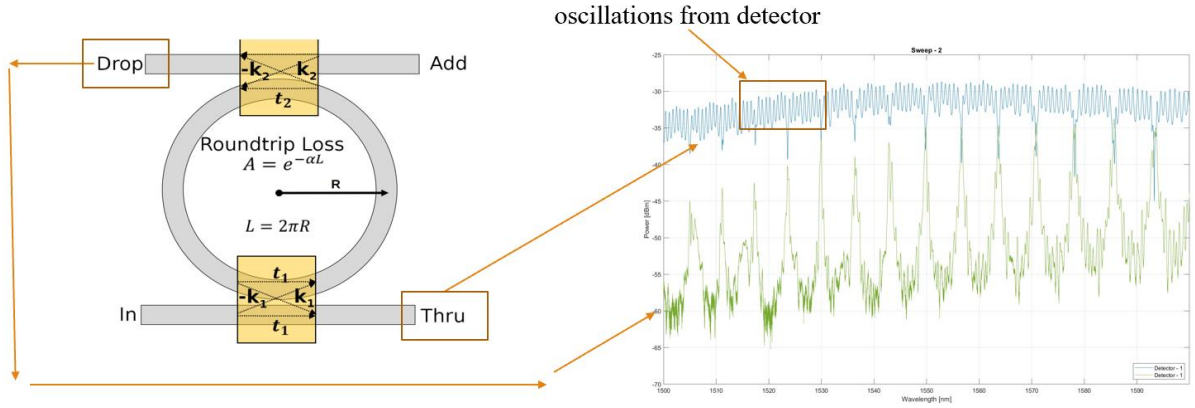


**Figure 5.4:** A double-bus ring resonator showing add and drop ports (left), response plot of a 300 nm double bus ring tested at RIT showing add and drop (right)

The response plot in Fig. 5.4 shows that total power of -30dBm (approximate y-axis reading) is obtained from the output grating coupler detector of the circuit out of a total 6dBm from the input source laser. The oscillations observed are just an anomaly (noise) from the detector and can be removed by fitting a polynomial equation for better reading. Anything below -60 dBm is just the noise floor of the detector. So, an ideal ring resonator in a critically coupled state should have no transmission coming out of the straight 'through' waveguide at a specific incoming wavelength of light. This critical coupling state can be observed in Fig. 5.5 (400 nm single bus ring) where, at ~1568 nm, the resonance goes straight into the 'loss' zone. The FSR was measured to be 7 nm.

The other resonances that are seen to terminate at different loss values are because of the varying coupling levels at different wavelengths. So, with a critically coupled response plot from a ring resonator, it is safe to assume that the resonances that are leading towards the critically coupled state are under-coupled and the resonances that are after the extinction mean that the circuit is over-coupled. The formula for Q factor in chapter Eq. implies that if

the ring loss in the circuit is less, the Q is high. Hence a good ring resonator circuit is expected to have a very low loss and high Q factor. Industry grade low loss ring resonators would be having Q values >25000. The circuits measured at RIT had an average Q of 5000 at 1550 nm.

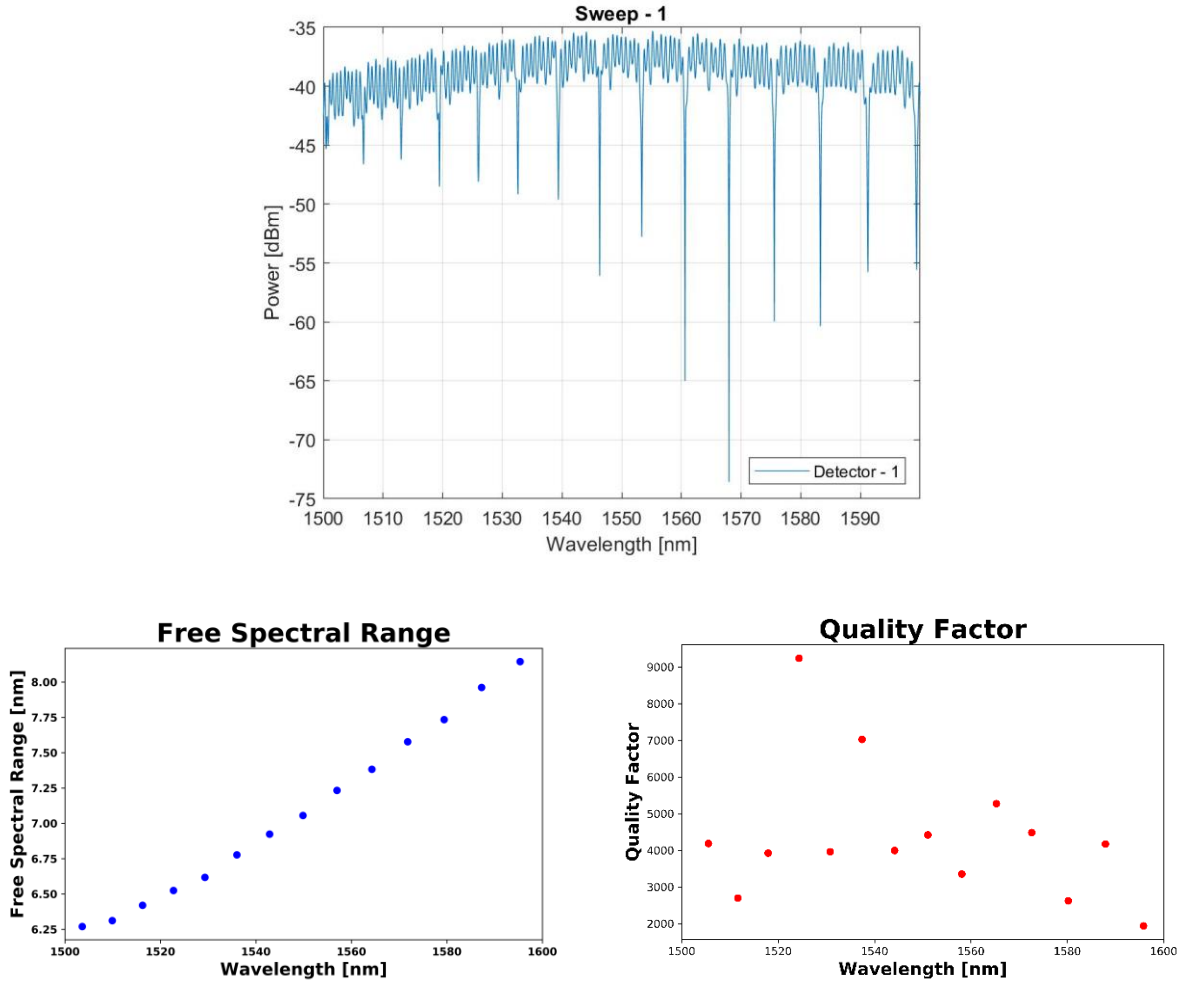


**Figure 5.5:** Response of a 400 nm single-bus ring resonator circuit (top). Extracted FSR value = 7 nm at 1550 nm (bottom left). Extracted Q = 4200 at 1550 nm

The extracted FSR from the circuit was 7 nm. Thermal modulation would now involve applying voltage to the contact probe pads and heating up the ring heater through joule heating as explained in chapter 2, section 2.4. After measuring the passive optical response

from the circuit, the electrical probes were lowered carefully onto the 50 µm x 50 µm pads to avoid damaging the probe tips and the pads. The probes were connected to a voltage source generator and an initial 1 V was supplied to the pads. The corresponding current reading was measured. The fiber array sweep was done again to couple light into the circuit to record any modulation effects. As expected, the resonances shifted by ~1 nm. The process was repeated by incrementing the voltages until a full 7 nm FSR shift was obtained. The total required voltage was ~6V as seen in Fig. 5.7. The corresponding power and resistance calculations were recorded in table 5.1. The power sweeps for voltage increments can be seen in Fig. 5.6.

**Table 5.1:** Resistance and Power calculations

| V | I (A) | Resistance (ohms) | Power (mW) |
|---|---|---|---|
| 1 | 0.0019 | 526.3157895 | 1.9 |
| 2 | 0.004 | 500 | 8 |
| 3 | 0.0056 | 535.7142857 | 16.8 |
| 4 | 0.007 | 571.4285714 | 28 |
| 5 | 0.0081 | 617.2839506 | 40.5 |
| 6 | 0.009 | 666.6666667 | 54 |
| 7 | 0.0098 | 714.2857143 | 68.6 |

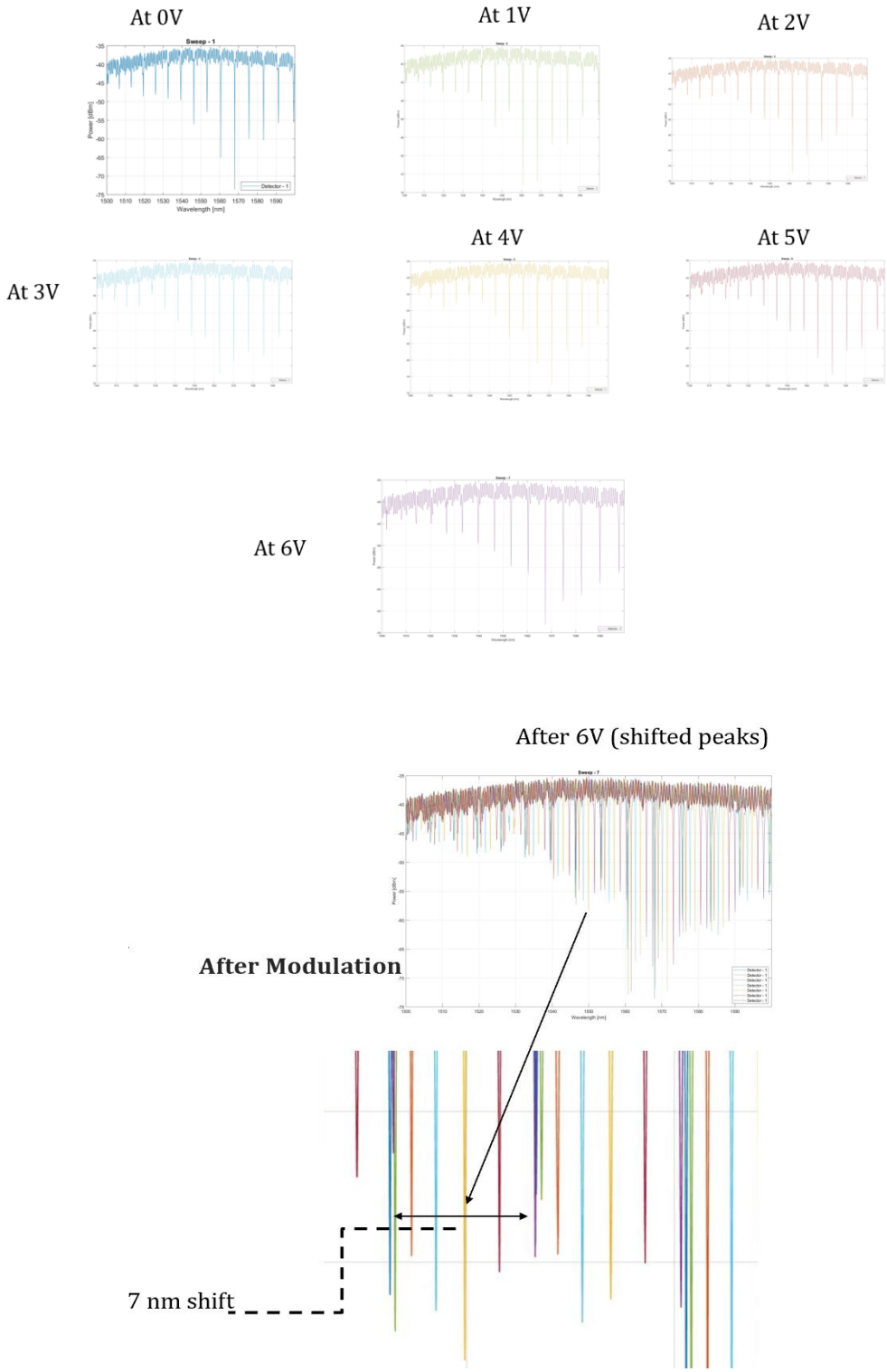


**Figure 5.6:** Individual responses (top), overlay after 6V supply showing 7 nm resonance shift (bottom).

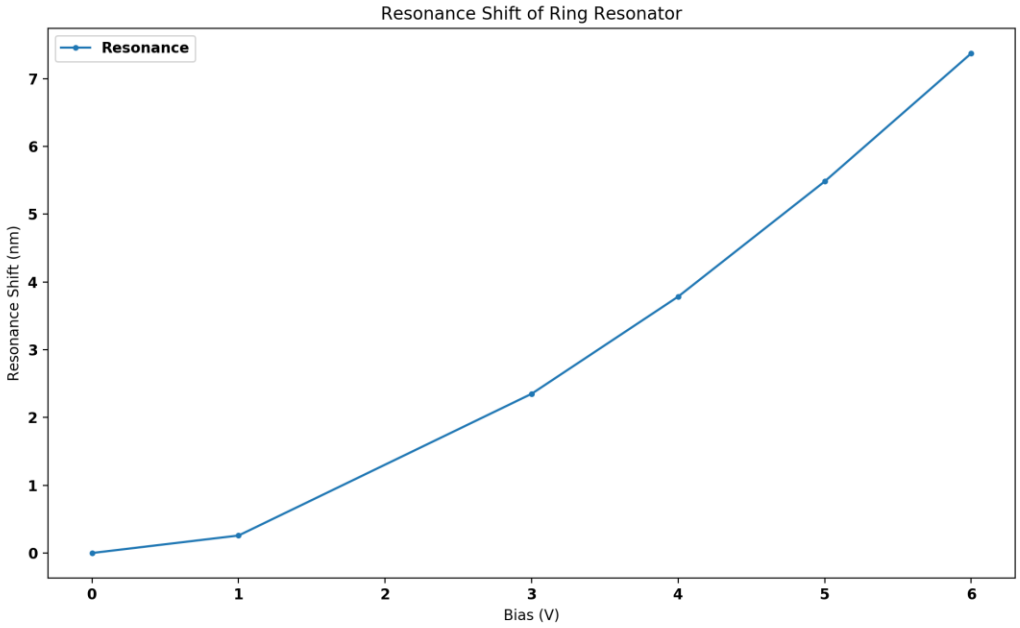


**Figure 5.7:** Resonance shift (nm) Vs Bias (V) showing full 7 nm FSR shift at 6V supply

# CONCLUSIONS AND FUTURE WORK

This thesis has successfully established the foundation process flow for active and passive photonic circuits fabrication and is a step further in advancing the fabrication curriculum of the existing photonic integrated circuits course at Rochester Institute of Technology (RIT).

Several optimizations and process changes can be added to increase the thermo-optic performance of the photonic heater circuits. Replacing titanium with a better resistive metal like Nichrome alloy would lower the circuit's power consumption. Instead of the established negative resist processing for heaters fabrication (in this thesis), the mask polarity can be inverted to get better aspect ratio heater features. Also, from the plots it is evident that the peaks continue to shift as power is supplied to the ring heater. In an attempt to find out the maximum tolerance for the heating circuit, power supply was increased until the metal started glowing red (Fig. 6.1). From modelling the heat transfer in Lumerical DEVICE solutions revealed that, to have a π phase response (modulation) to the original light mode, a power of 28 mW was required (refer [13] and Fig. 6.2 for prior heat transfer modelling work at RIT). At 28 mW in this thesis (table 5.1), the total FSR shift obtained was 3 nm (Fig. 5.6) and the total heat transferred to the silicon waveguide was 344K or 70˚C (Fig. 6.2).

More precise modelling can be done to determine the exact heat transfer parameters and simulate the total $n_{eff}$ change. Thermal imaging can be done to verify the actual temperature of the Titanium heater while the thermo-optic effect occurs. The actual fabrication results can be compared with modelling results to understand the optical losses and more fine tuning of the process can be done to improve the circuits' performance and overall results.

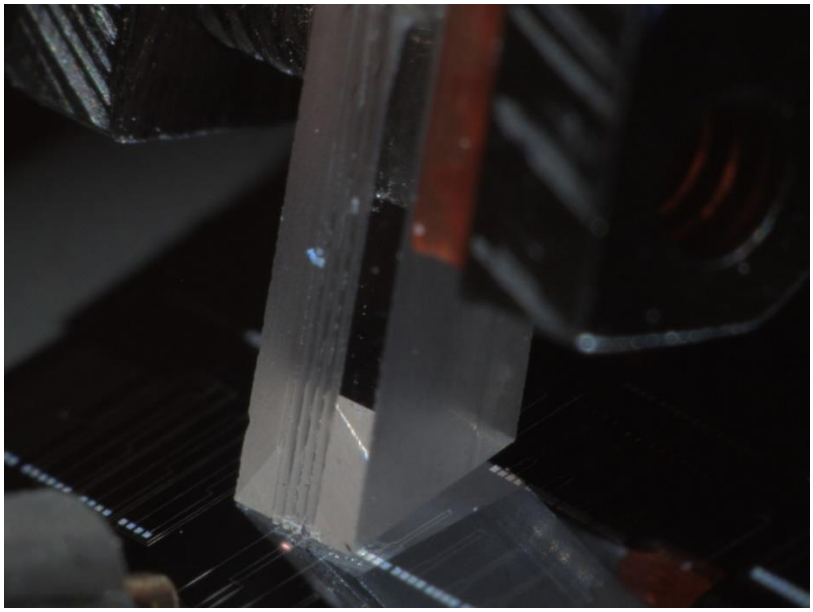

**Figure 6.1:** Titanium glow at 12V supply

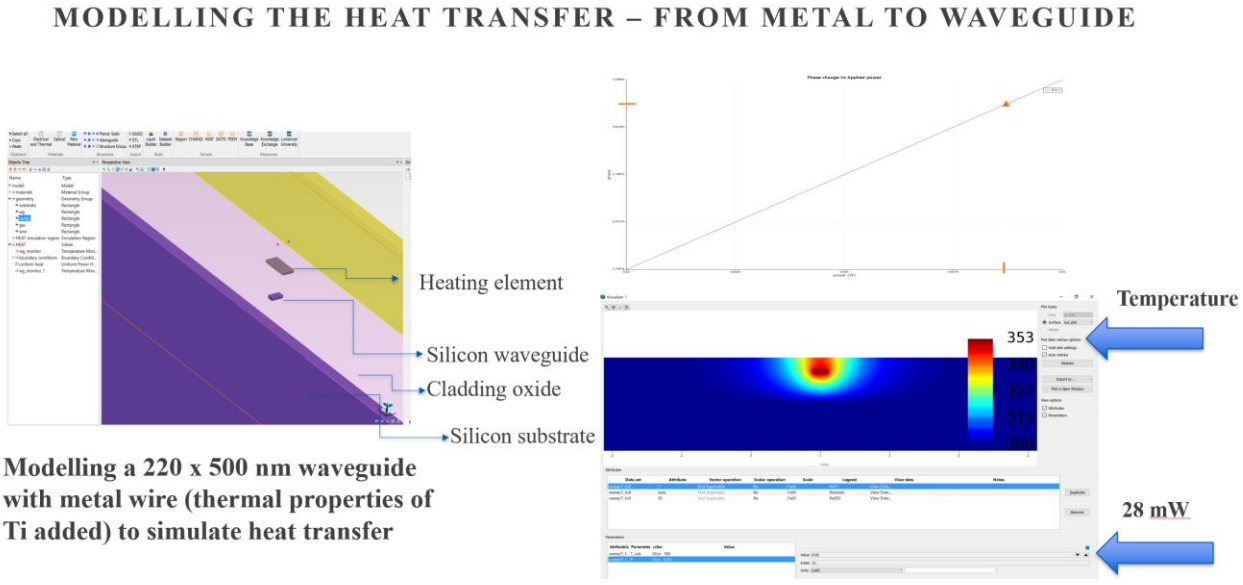


**Figure 6.2:** Prior work - Waveguide and heater modelling in Lumerical DEVICE (left), Power vs Phase change plot showing 3.14 change at 28 mW (right top), waveguide temperature at ~344K (right bottom) [13]

# REFERENCES


[1] What is telecom optical wavelength bands? | Fiberlabs Inc", Fiberlabs Inc, 2019. [Online]. Available: https://www.fiberlabs.com/glossary/about-optical-communication-band/. [Accessed: 11- Aug- 2019].

[2] S. Kumar and M. Deen, Fiber optic communications. West Sussex, United Kingdom: John Wiley & Sons, 2014.

[3] D. Vermeulen et al., "High-efficiency fiber-to-chip grating couplers realized using an advanced CMOS-compatible Silicon-On-Insulator platform", Optics Express, vol. 18, no. 17, p. 18278, 2010. Available: 10.1364/oe.18.018278.

[4] L. Chrostowski and M. Hochberg, Silicon Photonics Design. Cambridge: Cambridge University Press, 2015.

[5] D. Rabus, Integrated ring resonators. Berlin: Springer, 2007.

[6] S. Sivaram, Chemical vapor deposition. New York: Van Nostrand Reinhold,

[7] Engineering.dartmouth.edu, 2019. [Online]. Available: http://engineering.dartmouth.edu/microeng/processing/lithography/NR93000PY Exposure.pdf. [Accessed: 12- Aug- 2019].

[8] S. Wolf and R. Tauber, Silicon processing for the VLSI era. Sunset Beach: Lattice Press, 1990.

[9] Purdue.edu, 2019. [Online]. Available: https://purdue.edu/discoverypark/birck/files/Plasma_RIE_Etching_Fundamentals_and_Applications.pdf. [Accessed: 12- Aug- 2019].

[10] Microchem.com, 2019. [Online]. Available: http://www.microchem.com/pdf/IM-HM-140.pdf. [Accessed: 12- Aug- 2019].

[11] "waveguide cladding - Google Search", Google.com, 2019. [Online]. Available: https://www.google.com/search?q=waveguide+cladding&rlz=1C1CHBF_enUS813US813&source=lnms&tbm=isch&sa=X&ved=0ahUKEwiysrGr8anjAhVCGM0KHd89CV0Q_AUIESgC&biw=1500&bih=841#imgrc=Z4Q8G2tZ6Z3YWM: [Accessed: 12- Aug- 2019].

[12] "System — Maple Leaf", Maple Leaf, 2019. [Online]. Available: http://mapleleafphotonics.com/about#at-a-glance. [Accessed: 12- Aug- 2019].

[13] Deenadayalan, Venkatesh & Thomas, Paul & Preble, Stefan. (2019). Fabrication of Silicon photonic circuits with integrated thermo-optic heaters for education. 1-5. 10.1109/ASMC.2019.8791832.

[13] K. R. Williams, K. Gupta, and M. Wasilik, "Etch rates for micromachining processing-Part II," Journal of Microelectromechanical Systems, vol. 12, pp. 761-778, 2003

[14] S. Lakshminarayanamurthy, N. A. Rummage, N. A. Mogent, D. E. Ewbank, J. A. Steidle, M. L. Fanto, et al., "Silicon photonic wafer fabrication for education," in 2017 28th Annual SEMI Advanced Semiconductor Manufacturing Conference (ASMC), 2017, pp. 184-188

[15] Soref, R. and Larenzo, J. (1986). “All-silicon active and passive guided-wave components for λ = 1.3 and 1.6 μm”. IEEE Journal of Quantum Electronics, 22(6), pp.873-879

[16] Lukas Chrostowski, Zeqin Lu, Jonas Flueckiger, Xu Wang, Jackson Klein, Amy Liu, Jaspreet Jhoja, James Pond, "Design and simulation of silicon photonic schematics and layouts," Proc. SPIE 9891, Silicon Photonics and Photonic Integrated Circuits V, 989114 (May 13, 2016)

[17] Fiber Optic Communications: Fundamentals and Applications” by Shiva Kumar and M. Jamal Deen, John Wiley & Sons (US). (c) 2014. Copying Prohibited

[18] “Thermal rectification of integrated microheaters for microring resonators in silicon photonics platform” Meisam Bahadori, Student Member, IEEE, Alexander Gazman, Natalie Janosik, S´ebastien Rumley, Ziyi Zhu, Robert Polster, Qixiang Cheng, and Keren Bergman, Fellow, IEEE, Fellow, OSA

[19] MCSE 889 Photonic Integrated Circuits, Stefan Preble, Rochester Institute of Technology

[20] Lumerical solutions